1 **Melt inclusions in arclogitic xenoliths constrain the genesis of the lower continental arc**

2 **crust beneath the Northern Volcanic Zone, Colombia.**

3

4 **Omar Gianola**[1*], Benedetta Costa[1,‡], Fabio Ferri[1], Mattia Gilio[2], Maurizio Petrelli[3], Mara

5 Murri[2], Anna Barbaro[1], Matteo Alvaro[2], Andrés Rodríguez-Vargas[4], Stefano Poli[5], Bernardo

6 Cesare[1]

7 [1] Department of Geosciences, University of Padova, Via G. Gradenigo 6, 35131 Padova, Italy

8 [2] Department of Earth and Environmental Sciences, University of Pavia, Via A. Ferrata 1,

9 27100 Pavia, Italy

10 [3] Department of Physics and Geology, University of Perugia, Piazza dell'Università, 06123

11 Perugia, Italy

12 [4] Minerlab Limitada, Calle 51 Sur Nº 80i-34, Bogotá, D.C., Colombia

13 [5] Dipartimento di Scienze della Terra "Ardito Desio", Università degli Studi di Milano, Via

14 Mangiagalli 34, 20133, Milano, Italy

15

16 * Corresponding author. E-mail address: gianola@snsb.de

17

18 [‡] Present address: Institute of Material Technology, Building Physics and Building Ecology,

19 Faculty of Civil Engineering, Vienna University of Technology (TU Wien), Karlsplatz

20 13/207-01, A-1040 Vienna, Austria

21

22

23

28

29

ABSTRACT

31 Volcanic arcs above subduction zones are thought to be the principal locations where juvenile

32 magmatic crust forms and is refined to become continental crust with an andesitic

33 composition. During this refinement mechanism, the formation of dense garnet pyroxenites

34 (arclogites), represented by high-pressure cumulates and restites after partial melting, leads to

35 the delamination of the lower arc crust. The Mercaderes-Río Mayo area in southern Colombia

36 is the only known locality in an active volcanic arc where arclogitic xenoliths have been

37 recovered. These xenoliths are entrained in the Granatifera Tuff, a late Cenozoic volcanic

38 vent, and they mainly consist of garnet, clinopyroxene, amphibole, plagioclase, rarely

39 scapolite, and accessory mineral inclusions of rutile, apatite, zircons, and quartz. Moreover,

40 the arclogites are also characterized by the presence of melt inclusions (MI), which are

41 mainly found within garnet, but can be also observed in amphibole, plagioclase,

42 clinopyroxene, and scapolite. The glasses measured for the MI in garnet and scapolite

43 typically have SiO_2-contents >57 wt.%, ranging from andesite to rhyolite in composition.

44 Petrographic and geochemical investigations allowed to discriminate between cumulitic and

45 restitic arclogites, with the latter showing the concomitant presence of primary MI and quartz

46 inclusions within the peritectic garnets. Therefore, our study provides for the first time a

47 strong evidence, at the microscale, for the anatectic origin of some arclogitic xenoliths.

48 Pressure and temperature conditions for the studied arclogites were estimated by

49 intracrystalline geothermometry, elastic geothermobarometry, phase equilibria modelling and

50 classical Fe–Mg exchange between garnet and clinopyroxene. Results mainly fall within the

51 range 960-1150°C and 1.6-1.9 GPa for most samples. We suggest that the investigated

52 arclogites derive from the root of the active Colombian volcanic arc, where differentiation

53 processes from mantle-derived melts and lower crust anatexis occur in close association.

54

55 **INTRODUCTION**

56 Active volcanic arcs, both oceanic and continental, are the direct result of crustal recycling

57 along subduction zones. The devolatilization of dense subducting oceanic slabs lowers the

58 solidus of the overlying peridotitic mantle and triggers the production of predominantly

59 basaltic magmas, which chemically differentiate along their ascending paths and eventually

60 erupt at the surface. With an overall length of ~41.000 km (Schmidt & Poli, 2013), modern

61 active volcanic arcs contribute significantly to the formation of juvenile continental crust.

62 There is indeed sound evidence that the average composition of plutonic and volcanic rocks

63 generated in many volcanic arcs resembles the average composition of the continental crust

64 (Rudnick, 1995; Taylor & McLennan, 1995; Jagoutz & Schmidt, 2012), highlighting the

65 pivotal role played by arc magmatic processes in the formation of modern continental crust.

66 Despite this gross similarity, it has been noticed that the chemical composition of the lower

67 arc crust largely differs from that of continents at comparable depths (Jagoutz & Behn, 2013;

68 Hacker et al., 2015; Kelemen et al., 2016) and therefore some refinement mechanisms are

69 necessary to transform arc crust into the continental crust. The two most accredited processes

70 responsible for the lower arc crust refinement are thought to be delamination of dense arc

71 rocks and relamination of more buoyant material from the subduction zone. Relamination is

72 inferred to take place in different ways and principally it might involve the emplacement of

73 less dense material at the base of the arc crust. This less dense material may have different

74 origins and compositions, including subducted sediments, subducted intra-oceanic arc

75 sections, portions of crust removed from the overriding plate or subducted continental crust

76   (e.g., Hacker et al., 2011; Kelemen et al., 2016). By contrast, delamination is a density sorting

77   effect in which dense magmatic arc cumulates or granulite- to eclogite-facies metamorphosed

78   arc lithologies become gravitationally unstable and sink into the underlying mantle (e.g.,

79   Jagoutz & Schmidt, 2013; Jagoutz & Kelemen, 2015). The delaminating rocks mainly consist

80   of garnet, pyroxene, amphibole, and Fe-Ti oxides and are often grouped under the descriptive

81   name of arclogites (Lee & Anderson, 2015; Ducea et al., 2021a). The twofold origin

82   (cumulate vs. restite) of arclogitic assemblages is extensively debated (Tatsumi, 2000; Lee et

83   al., 2006; Ducea et al., 2021a), and there are no unequivocal criteria for its assessment.

84   Determining the chemical composition and structure of the lower arc crust is not an easy task

85   since few locations in the world offer an adequate exposure of tilted arc roots. Among these,

86   particularly relevant are the Kohistan (N-Pakistan; e.g., Garrido et al., 2006; Burg, 2011;

87   Jagoutz & Schmidt, 2012) and the Talkeetna (S-Alaska; e.g., Greene et al., 2006; DeBari &

88   Greene, 2011; Kelemen et al., 2014) paleo-arcs, as archetypes for intra-oceanic arcs, and the

89   southern Sierra Nevada (W-USA; e.g., Saleeby, 1990; Klein & Jagoutz, 2021) and the Sierra

90   de Valle Fértil (W-Argentina; e.g., Otamendi et al., 2012; Ducea et al., 2015), as examples of

91   continental arc sections. Additional knowledge can also be acquired by the study of mafic

92   (i.e., 'arclogitic') and felsic xenoliths entrained in volcanic rocks. Although xenoliths tell

93   little about the structure of the lower arc edifice, they are not affected by metamorphic re-

94   equilibration due to late tectonic events and hence they provide invaluable information on the

95   mineral assemblage and chemical composition of the lower arc crust. Several localities

96   worldwide host lower arc crustal xenoliths (e.g., Ducea et al., 2021a) but one of them, the

97   Mercaderes-Río Mayo area in SW Colombia, is of particular interest because it is the only

98   known location where lower crustal xenoliths derive from an active Andean-type arc (Weber

99   et al., 2002; Rodríguez-Vargas et al., 2005; Bloch et al., 2017). In this area, volcanic tuffs

100   contain mantle and crustal xenoliths, allowing to probe and investigate the entire column

101   above the down-going oceanic slab.

102   In this study, we focus on some crustal xenoliths recovered from the Mercaderes-Río Mayo

103   area, as they provide unique clues to the differentiation and re-working processes that

104   characterize the root of an active continental arc. Melt inclusions hosted in their rock-forming

105   minerals (in particular garnet) helped to constrain the origin of these arclogites, some of

106   which are interpreted as restites, whereas elastic thermobarometry allowed to establish the

107   depths and temperatures at which the xenoliths resided before being incorporated in the

108   ascending magma. We also provide evidence that growth and 'maturation' of a lower arc root

109   are determined by the interplay between fractional crystallization from mantle-derived melts

110   and partial melting of crustal metabasaltic precursors.

111

112   **GEOLOGICAL SETTING**

113   The Andean Cordillera is a subduction-related active volcanic chain that can be subdivided,

114   from south to north, into 4 distinct zones, the Austral Volcanic Zone, the Southern Volcanic

115   Zone, the Central Volcanic Zone, and the Northern Volcanic Zone (NVZ). The NVZ

116   comprises the modern active-arc section located between central Ecuador and central

117   Colombia, approximately from 1°S to 7°N, and is bounded by the Colombian flat slab to the

118   north and the Peruvian flat slab to the south (Syracuse et al., 2016).

119   The Colombian territory can then be divided into three parallel Cordilleras elongated

120   approximately NE-SW, the Western, the Central, and the Eastern Cordillera, produced by

121   superposition of multiple orogenic events occurring since the Palaeozoic to the present. The

122   Western Cordillera has an oceanic affinity and is separated from the Central and Eastern

123   Cordilleras, both with a continental affinity, by the Romeral Fault System (RFS). The latter,

124   in the area of investigation, is identified as the Cauca – Almaguer fault and possibly

125 represents a subduction zone of continental-ocean type, which was blocked by the thick,

126 buoyant plateau, enabling subduction to migrate once more to the west. Few episodes of

127 crustal growth occurred with the generation of igneous bodies from the Jurassic to the

128 Neogene (Taboada et al., 2000). Seismic investigations with V_p and V_s have shown that in the

129 Mercaderes-Río Mayo area the crustal thickness ranges between 50 and 70 km, with an arc

130 root that possibly is 13 to 20 km thick (Poveda et al., 2015; Avellaneda-Jiménez & Monsalve,

131 2022).

132 The Mercaderes-Río Mayo area carries the famous lower crustal and mantle xenoliths

133 recovered within the Granatifera tuff formation. This area (Fig. 1) is characterized by a

134 complex lithologic sequence including metasedimentary rocks of the paleozoic Arquía

135 Complex; metavolcanis and metasedimentary units of the Cretaceous Diabásico Group;

136 sedimentary rocks of the Mosquera–Esmita Formation and pyroclastic rocks of the Galeón

137 Formation with tertiary-quaternary age. All these units were intruded by the tertiary

138 porphyritic volcanics of dacitic and andesitic composition (Murcia & Cepeda, 1991; Weber,

139 1998). The metasediments and metavolcanics are in turn capped by the ~300 m-thick

140 Granatifera Tuff, which is thought to represent an eroded tuff cone or tuff ring (Weber et al.,

141 2002). Rodríguez-Vargas et al. (2005) suggested that the emission vent of the Granatifera

142 Tuff is reasonably located few hundred meters from the village of Higuerones, where the

143 volcanic edifice is partly preserved in the form of a caldera.

144 The Granatifera Tuff is divided into three main parts with the basal section composed of

145 volcanic breccias, agglomerates and lapilli tuffs, overlain by lithified tuffs, ash deposits and

146 debris flows (Weber et al., 2002; Rodríguez-Vargas et al., 2005).

147 The crustal and mantle xenoliths within the Granatifera Tuff are up to 20 cm in diameter and

148 include garnet-bearing rocks ranging from peridotites to websterites as most common mantle

149 xenoliths, garnet-free websterites and minor amounts of spinel-bearing mantle xenoliths. The

150   lower crustal xenoliths comprise a variety of amphibolites, pyroxenites, granulites, and

151   gneisses, metamorphosed under amphibolite to granulite facies conditions. According to Lu-

152   Hf dating, the xenoliths are younger than 5 Ma and may represent fragments of the lowermost

153   arc root and the underlying mantle wedge (Bloch et al., 2017).

154

155

156

157   **ANALYTICAL METHODS**

158   Back-scattered electron (BSE) images and semi-quantitative energy dispersive spectroscopy

159   (EDS) analyses of melt inclusions (MI) were carried out with a CamScan MX2500 Scanning

160   Electron Microscope (SEM), at the Department of Geosciences of the University of Padova

161   (Italy) and with a FEI Quanta 200 at CEASC (Centro di Analisi e Servizi per la

162   Certificazione, University of Padova).

163   Major element compositions of glasses and minerals were determined with a JEOL

164   JXA−8200 Superprobe electron probe micro-analyser (EPMA), equipped with five

165   wavelength dispersive spectrometers, at the Department of Earth Sciences (University of

166   Milano, Italy), employing an acceleration voltage of 15 kV, a beam current of 5 or 15 nA and

167   beam diameter of 1 μm (enlarged up to 10 μm for some analyses). Acquisition times were 10

168   s on peak and 5 s for background, measuring Na and K first to minimize diffusional losses.

169   Natural and synthetic minerals and glasses from the Smithsonian Microbeam Standards

170   (Jarosewich et al., 1980; Jarosewich 2002) and from Ingamells (1978) were used as elemental

171   standards and to monitor the analytical reproducibility. Si and Ca were measured on

172   grossular, Mg on olivine, Al on anorthite, Ti on ilmenite, Mn on rhodonite, Fe on fayalite, Cr

173   on pure chromium, Na on omphacite, K on K-feldspar, P on a Y-phosphate and S on

174   celestine. For glasses analysed in the xenoliths, alkali concentrations were corrected using

175 conservative factors obtained by the analysis of hydrous and anhydrous leucogranitic glasses

176 of known composition. In this study we employed a 10.1 wt.% H_2O-bearing glass (LGB 2;

177 Behrens & Jantos, 2001), a 5.5 wt.% H_2O-bearing glass (DL; Acosta-Vigil et al., 2003) and a

178 nearly anhydrous (H_2O = 300 ± 42 µg/g, 2 s.e.m.) glass (B; Morgan & London, 2005). Glass

179 and mineral standards are reported in Supplementary Table S1.

180 Laser ablation inductively coupled mass spectrometer (LA-ICP-MS) measurements of trace

181 elements in glasses were performed at the Department of Physics and Geology, University of

182 Perugia (Italy) using a Teledyne Photon Machine G2 laser ablation device coupled to a

183 Thermo Fischer Scientific iCAP Q quadrupole mass spectrometer. Trace element

184 concentrations in the unknowns were calibrated against NIST SRM 610 as external standard

185 and the USGS BCR2G reference material was processed as an unknown to assess the quality

186 of the measurements and the accuracy of the calculations. Under the reported analytical

187 conditions, precision and accuracy values are typically below 10 % (Petrelli et al., 2016a,b).

188 Analyses were conducted using a classical sample-standard bracketing, where NIST SRM

189 610 was measured twice every 12-15 samples. Both standard and unknowns were ablated

190 using a circular spot with a diameter of 15 µm (except for one sample where a spot size of 25

191 µm was employed), a repetition rate of 10 Hz and an energy density of 3-4 J/cm^2. Ablation

192 times were 30 s per spot, preceded by a 30 s background measurement and followed by 20 s

193 of washout. Si was used as internal standard and measured intensities were then converted

194 into concentrations using the Iolite 3 software (Paton et al., 2011). Conservatively, elements

195 that are strongly enriched in the host garnet (heavy rare earth elements, Y, Sc, V and Mn)

196 were not considered for the analysed glasses of the melt inclusions, in order to avoid any

197 artefact value that may derive from the possible mixed analysis with the host. The complete

198 trace elements dataset can be found in Supplementary Table S2.

199   Raman spectra of quartz and zircon inclusions in garnet were measured at the University of

200   Pavia with a Horiba LabRam HR Evolution spectrometer (holographic gratings of 1800

201   grooves/mm) equipped with an Olympus BX41 confocal microscope at controlled

202   temperature of 20 ± 1 °C. Raman spectra were excited using the 532 nm line of a solid state

203   (YAG) laser. The laser power on the sample surface was approximately 1-2 mW. The

204   spectrometer was calibrated to the Raman peak of silicon at 520.5 cm^{-1}. We used spectra of

205   free crystals with the same composition as the inclusions as further calibration for the entire

206   spectral range used in our investigation. The collected spectra were baseline-corrected for the

207   continuum luminescence background when necessary, temperature-reduced to account for the

208   Bose-Einstein occupation factor (Kuzmany, 2009) and normalized to the acquisition time.

209   Peak positions, full widths at half maximum (FWHMs), and integrated intensities were

210   assessed from fits with pseudo-Voigt functions. For each of the selected Raman bands we

211   determined the shift $\Delta\omega$ of the Raman band as the difference between the Raman shift of the

212   inclusion ω_i from that of an unstrained reference crystal (ω_0). As standards, we used free

213   (unstrained) quartz (mineralogical collection University of Pavia) and zircon (Mud Tank Hill,

214   Australia) crystals, measured multiple times during each measurement session at ambient

215   pressure and room temperature to eliminate shifts in peak positions due to instrumental drift

216   and/or minor changes in room temperature. The ω_0 values were averaged and then subtracted

217   from the ω_i of the strained inclusions analysed in between two consecutive standard

218   measurements. For zircon inclusions, because of the possible misinterpretations due to effects

219   of radiation damages (which change the elastic properties of zircon causing shifting and

220   broadening of the Raman peaks, Binvignat et al., 2018), we adopted the procedure described

221   in Campomenosi et al. (2020). Therefore, we included in the analysis only inclusions with

222   full widths at half-maximum (FWHM) for the 1014 Raman band smaller than $\omega_{1014}^{FWHM} <$

223    $5.0 \; cm^{-1}$. The $\Delta\omega$ values of each mode of zircon and quartz inclusions and unstrained

224   standards are listed in the supplementary material (Supplementary Table S3). Finally, sets of

225     $\Delta\omega$ for each inclusion (modes ω_{128}, ω_{206}, ω_{265}, and ω_{464} for quartz and modes ω_{438}, ω_{969}, ω_{1014}

226   for zircon, as they are generally unaffected by overlap with modes of the host garnet and have

227   no significant shifts due to changes in composition) have been used to determine strain using

228   the software stRAinMAN (Angel et al., 2019) by employing the Grüneisen tensors for quartz

229   (Murri et al., 2018a) and zircon (Stangarone et al., 2019). The differences of the thermo-

230   elastic properties of a host-inclusion pair system may lead to the development of residual

231   pressures upon exhumation (Rosenfeld & Chase, 1961; Angel et al., 2014). Knowing the

232   inclusion pressure (P_{inc}) at T_0 (25 °C) and the thermodynamic properties of host and inclusion

233   one can back-calculate a line of possible entrapment conditions in the P-T space: the isomeke

234   (Rosenfeld & Chase, 1961; Angel et al., 2014; Angel et al., 2017b). The entrapment isomekes

235   for quartz and zircon inclusions were obtained from the strains with the software EntraPT

236   (Mazzucchelli et al., 2021), using the equation of state of quartz (Angel et al., 2017a), zircon

237   (Ehlers et al., 2022) and garnet end-members (Angel et al., 2022). The isomekes were then

238   corrected for garnet composition following the method described in Angel et al. (2022). The

239   strain of each inclusion was converted to stress using the elastic tensors at room P-T for

240   quartz (Wang et al., 2015) and zircon (Özkan et al., 1974). The P_{inc} was calculated from the

241   stress tensor as the mean normal stress ($P_{inc} = (\sigma_1 + \sigma_2 + \sigma_3)/3$). The uncertainty on P_{inc} of each

242   inclusion was propagated from the uncertainty on strain using the respective elastic tensor by

243   the software EntraPT, through the procedure described in Mazzucchelli et al. (2021). To

244   avoid the effects of strain localization at corners and inclusion shape effects (Mazzucchelli et

245   al., 2018; Campomenosi et al., 2020), each Raman measurement was performed at the centre

246   of well-rounded quartz and zircon inclusions.

247   Single-crystal X-ray diffraction data collections, followed by structural refinements with

248   chemical constraints, were carried out on seven pyroxene single crystals from the sample

249 18XC10 in order to determine the closure temperatures related to the Fe^{2+}-Mg exchange

250 reaction (Ganguly, 1982). X-ray diffraction data collections have been carried out using a

251 Rigaku-Oxford Diffraction Supernova diffractometer available at the Department of

252 Geosciences, University of Padova. The instrument is a kappa-geometry goniometer

253 equipped with an X-ray micro-source, MoK_α ($\lambda = 0.71073$ Å) operating at 50 kV and 0.8 mA

254 (power = 40 W) and a Pilatus 200 K Dectris area detector. Data collections and data

255 reduction, including intensity integration together with background and Lorentz-polarization

256 corrections, have been performed using the Crysalis software (Rigaku-Oxford-Diffraction©)

257 package. The unit-cell parameters with the discrepancy indices R_{int}, R_{all}, R_w on all the

258 observed structure factors (F_o^2) and the goodness of fit (S) of the structure refinements with

259 chemical constraints for the seven crystals are reported in the Supplementary Table S4

260 together with the mean atomic numbers (m.a.n.) in electrons per formula unit (e.p.f.u.) at the

261 crystallographic sites (*M*1, *M*2, *M*21) obtained when the structure refinement reached

262 convergence, before introducing the chemical constraints. For all samples the calculated

263 mean atomic numbers from the unconstrained refinements agree within two standard

264 deviations with the values of electrons per formula unit (e.p.f.u.) calculated from the EPMA

265 (Supplementary Table S4). Therefore, this enabled us to use the results from the EPMA as

266 chemical constraints for the structural refinements, following the procedure and taking into

267 account the same constraints as in Domeneghetti et al. (2013), in order to determine the

268 clinopyroxene site distribution (assuming one standard deviation as the error). The structure

269 refinements with chemical constraints have been carried out following the procedure reported

270 in Murri et al. (2018b) and Murri et al. (2019) by using the SHELX-97 program (Sheldrick,

271 2008). The site populations obtained from the structural refinements with chemical

272 constraints and the distribution coefficients (k_D), with their relative errors, are reported in the

273 Supplementary Table S4. Errors on k_D were calculated by standard error propagation.

274 The P-T conditions for sample 18XC10 were also investigated by phase equilibria modelling

275 for the chemical systems CaNaKFMASHTiMn. The bulk rock composition was estimated by

276 combining the modal mineral proportions obtained from a compositional SEM map and the

277 mineral compositions measured by EPMA (see below). Due to the nearly dry nature of the

278 rock, it has been assumed that the only source of water was amphibole and therefore

279 calculations were performed with a H_2O content of 0.04 wt.%. Stability fields of coexisting

280 minerals were outlined by Gibbs free energy minimization using the Perple_X software

281 package (version 6.9.1; Connolly 2005, 2009). Calculations take into account solution models

282 for the following phases: clinopyroxene, amphibole, and melt (Green et al., 2016), garnet and

283 orthopyroxene (White et al., 2014), feldspar (Holland & Powell, 2003), spinel (White et al.,

284 2002), and ilmenite (White et al., 2000).

285

286 **RESULTS**

287 **Mineral assemblages**

288 We studied four samples, 3-5 cm in size, representative of the crustal xenoliths: 18XC1,

289 18XC5, 18XC10 and 18XC20 (Supplementary Fig. S1a-d). They broadly encompass the

290 categories of Grt-Px hornblendites (mineral abbreviations after Whitney & Evans, 2010),

291 pyribolites and pyroxenites as defined by Weber et al. (2002) and can also be collectively

292 defined as arclogites according to the criteria of Ducea et al. (2021a).

293 Sample 18XC1 contains, in order of decreasing abundance, garnet, plagioclase, amphibole,

294 clinopyroxene, and rare scapolite. The texture is slightly layered, inequigranular interlobate,

295 with an average grain-size of 1-2 mm, where rare garnet crystals may reach 7 mm. All grain

296 boundaries display evidence of reaction between adjacent minerals and of infiltration of

297 external melt (Fig. 2a). In some cases, the minerals may be intensely altered or transformed

298 (e.g., pyroxene into amphibole). In places, subhedral crystals of plagioclase with planar

ORIGINAL UNEDITED MANUSCRIPT

299 crystal faces (Fig. 2b) indicate crystallization from a melt (Sawyer, 2008). Melt inclusions

300 have been observed in garnet and in the cores of plagioclase. The modal composition for

301 18XC1, determined through a SEM compositional map from a thick section (see

302 Supplementary Fig. S2a), is: 36.1 vol.% garnet, 12.4 vol.% clinopyroxene, 27.0 vol.%

303 plagioclase, 22.8 vol.% amphibole, 1.3 vol.% scapolite, 0.2 vol.% apatite and 0.1 vol.%

304 rutile.

305 Sample 18XC5 consists of garnet, amphibole, clinopyroxene and rare plagioclase and

306 scapolite. It has an isotropic granoblastic microstructure where the coarser mineral, anhedral

307 garnet, may reach 4 mm in size (Supplementary Fig. S1b). Microstructural relationships

308 suggest that crystallization of garnet and clinopyroxene was coeval, followed by interstitial

309 amphibole and plagioclase. Like in the previous sample and in most xenoliths from

310 Mercaderes, 18XC5 displays evidence of pervasive reaction at all grain boundaries (Fig. 2c),

311 probably related to entrainment in the lava. Quartz occurs as rare inclusions in garnet (Fig.

312 2d; see below).

313 Sample 18XC10 is a pyroxenite dominated by garnet, pyroxene and plagioclase, with minor,

314 heterogeneously distributed hornblende (Supplementary Fig. S1c). The rock is fine-grained,

315 with average grain-size of 1 mm, and displays a mineralogical banding highlighted by 2-3

316 mm-thick monomineralic garnet layers (Supplementary Fig. S1c). The microstructure is

317 granoblastic and the monomineralic garnet layers show a polygonal texture derived from the

318 impingement of growing grains. Unlike most of the crustal xenoliths from Mercaderes,

319 sample 18XC10 displays a well-equilibrated texture (Fig. 2e), with neither sign of reaction

320 between adjacent minerals, nor of interaction with (or infiltration of) melt from the host lava.

321 Igneous microstructures pointing to crystallization from melt are rarely observed and

322 represented by plagioclase with crystal faces. The studied sections consist of two distinct

323 zones (see Supplementary Fig. S2b) separated by a garnet rich layer: zone 1 consists of

324 garnet, clinopyroxene, and plagioclase in nearly equal amount with minor pargasitic

325 amphibole; zone 2 mainly consists of garnet and clinopyroxene with interstitial plagioclase.

326 Accessory rutile and apatite are equally distributed in both zones. The modal compositions

327 for the two zones of sample 18XC10, determined through a SEM compositional map from an

328 entire thin section (see Supplementary Fig. S2b), are: 37.8 vol.% garnet, 33.4 vol.%

329 clinopyroxene, 25.3 vol.% plagioclase, 3.2 vol.% amphibole and 0.3 vol.% rutile for zone1,

330 and 58.1 vol.% garnet, 23.9 vol.% clinopyroxene, 15.8 vol.% plagioclase, 1.6 vol.% apatite

331 and 0.6 vol.% rutile for zone 2. Quartz is present only as inclusions in garnet (Fig. 2f).

332 Sample 18XC20 is a banded xenolith with different Amp/Pl ratios. Garnet is abundant in both

333 bands, whereas clinopyroxene is scarce. Although amphibole is the most abundant and

334 coarser mineral, reaching up to 4 mm in size, it also occurs as inclusions in garnet and

335 clinopyroxene. Garnet has a maximum diameter of 2 mm and may contain glass inclusions.

336 Also plagioclase contains glass inclusions and, where abundant, displays euhedral shapes or

337 interstitial positions (Fig. 2g), suggestive of crystallization from melt. This xenolith shows

338 little evidence of reaction or resorption of crystals at grain boundaries, which are in most

339 cases clean and well-preserved. Quartz is present only as inclusions in garnet (Fig. 2h).

340 All samples contain rutile as accessory phase (Supplementary Fig. S1i), and all contain

341 apatite.

342

343 **Melt and mineral inclusions**

344 Several types of inclusions occur in the main minerals of the studied xenoliths. We focus

345 primarily on the inclusions hosted in garnet, as they are the object of further analyses and

346 constrain the thermobarometric estimates and petrogenetic discussion made below. An

347 extensive documentary of backscattered SEM images of melt inclusions (MI) is reported in

348 the supplementary material (Supplementary Fig. S3).

349 Melt inclusions occur in garnet crystals from all samples. They are rare in 18XC1 and

350 18XC5, common in 18XC20, abundant in 18XC10. Their textural position, either isolated or

351 scattered within the host, or more commonly arranged in the garnet cores (zonal arrangement

352 after Roedder, 1984) indicates that the MI are primary in origin, i.e., they were trapped by the

353 growing garnet (Fig. 3a, b). Occasional secondary MI locally form planar arrays. MI often

354 display a negative crystal shape, more rarely rounded, and their size is generally <40 μm,

355 with few larger MI reaching 100 μm (Fig. 3c-f). In samples 18XC10 and 18XC20, where MI

356 in garnet are more abundant, they contain a single or multiple shrinkage bubbles (Fig. 3d, e;

357 Roedder, 1984), and local evidence of necking-down (Fig. 3d, f). The glass is optically fresh

358 and colourless in 18XC10, whereas in 18XC20 it is more turbid and browner in colour (Fig.

359 3g). Under SEM imaging the MI in 18XC1, 18XC10 and 18XC20 often display the presence

360 of nanolites made of a heavier phase (Fig. 3h and Supplementary Fig. S9).

361 MI occur in plagioclase from 18XC1 (Fig. 3i) and 18XC5, where they are respectively

362 primary and secondary in origin. Very rarely they are also observed in clinopyroxene from

363 18XC5 and 18XC10. In the latter sample the microstructures suggest a primary entrapment

364 (Supplementary Fig. S1g). MI have also been observed in amphibole from 18XC1, where

365 they display a tubular shape and appear secondary in origin (Supplementary Fig. S1h).

366 Finally, SEM imaging allowed to detect MI also in oxide minerals such as rutile in 18XC1

367 (Fig. 3j). SEM also revealed the common occurrence of minute offshoots at MI boundaries,

368 suggestive of overpressuring of the inclusions either by heating after entrapment or by

369 decompression of the xenoliths during magma ascent.

370 MI may contain quartz (Fig. 3f) and rutile as trapped minerals, i.e., crystals which were

371 already present at the time of inclusion entrapment (Supplementary Fig. S1f, i).

372 Rutile occurs as solid inclusion in garnet in all samples, whereas zircon and quartz are

373 observed in all except 18XC1. Rutile is observed both as small, crystallographically arranged

374 needles suggesting exsolution from garnet, and as coarser crystals with variable aspect ratio

375 (Fig. 3a, b; Supplementary Fig. S1i). In sample 18XC10, the rutile needles are located in a

376 brownish intermediate annulus separating the inclusion-rich core from inclusion-free or

377 inclusion-poor rims (Fig. 3b; Supplementary Fig. S1i). Zircon inclusions are particularly

378 abundant, where they occur as crystals with 20-30 μm average size mostly located in the

379 garnet cores.

380 Quartz inclusions in garnet are a key microstructure of most of the investigated crustal

381 xenoliths at Mercaderes (Fig. 3a, b, f, k and Supplementary Fig. S1f), and their association

382 with MI had already been highlighted by Weber et al. (2002). Quartz inclusions range from

383 rare and scattered to very abundant, and display size from 10 to 150 μm. The shape of quartz

384 inclusions ranges from spherical to slightly elongate, and in places quartz inclusions display a

385 strong shape preferred orientation (Fig. 2f and Fig. 3b). When observed in detail, quartz

386 inclusions in garnet are faceted (Fig. 3k), as common in (U)HT rocks displaying shape

387 maturation features (Cesare et al., 2021).

388

389 **Mineral chemistry**

390 The complete dataset for the mineral chemistry of the analysed samples is reported in the

391 Supplementary Table S5. Chemical analyses of garnets in sample 18XC1 (Fig. 4a) show that

392 some crystals are slightly zoned, whereas some others display a marked zoning between core

393 and rims. The slightly zoned minerals are characterized by subtle Fe-richer core compositions

394 ($Alm_{36-40}Pyr_{29-34}Grs_{29-31}Sps_{0-1}$) compared to rims ($Alm_{34-38}Pyr_{30-31}Grs_{31-35}Sps_{0-1}$), whereas

395 cores and rims in the zoned garnets are $Alm_{39-53}Pyr_{23-34}Grs_{22-31}Sps_{0-2}$ and $Alm_{32-39}Pyr_{29-31}Grs_{31-36}Sps_{0-1}$,

396 $_{31}Grs_{31-36}Sps_{0-1}$, respectively. Garnets in 18XC5 are Mg-richer (Fig. 4b) and do not show any

397 zoning between cores ($Alm_{32-35}Pyr_{43-46}Grs_{21-23}Sps_{0-1}$) and rims ($Alm_{31-34}Pyr_{44-49}Grs_{19-21}Sps_{0-1}$)

398 $_1$). Garnets in 18XC10 are dominated by the almandine and pyrope components (Fig. 4c) and

ORIGINAL UNEDITED MANUSCRIPT

399 display a weak zoning in the grossular component between cores ($Alm_{38-42}Pyr_{38-43}Grs_{17-22}Sps_{0-1}$)

400 and rims ($Alm_{38-43}Pyr_{40-44}Grs_{16-17}Sps_{0-1}$). In sample 18XC20 both homogeneous and

401 zoned garnets have been observed. The zoned garnets (Fig. 4d) have cores slightly richer in

402 Fe ($Alm_{47-49}Pyr_{27-29}Grs_{21-22}Sps_{2-3}$) compared to the rims ($Alm_{42-44}Pyr_{27-31}Grs_{26-27}Sps_{1-2}$), while

403 the homogeneous garnets have cores with $Alm_{44-46}Pyr_{26-29}Grs_{25-26}Sps_{1-2}$ and rims with $Alm_{42-45}Pyr_{27-32}Grs_{24-28}Sps_{1-2}$.

404 $_{45}Pyr_{27-32}Grs_{24-28}Sps_{1-2}$.

405 Clinopyroxene crystals in sample 18XC1 (Fig. 5a) show a very weak zoning, with Al-richer

406 (Al = 0.56-0.62 atoms per formula unit, a.p.f.u.) and lower X_{Mg} (X_{Mg}= 0.61-0.68, with X_{Mg}

407 expressed hereafter as [$Mg/(Mg+Fe^{TOT})$]) rims compared to cores (Al = 0.52-0.57 a.p.f.u. and

408 X_{Mg} = 0.66-0.69). On the other hand, the jadeite component (Jd) remains nearly constant

409 between rims and cores (0.11-0.14 a.p.f.u.). From a stoichiometric point of view Cpx cores

410 correspond to a composition equal to $Na_{0.11-0.14}Ca_{0.81-0.83}Al_{0.52-0.57}Fe_{0.23-0.26}Mg_{0.49-0.53}Si_{1.68-1.75}O_6$,

411 $_{1.75}O_6$, whereas rims can be defined as $Na_{0.11-0.13}Ca_{0.74-0.82}Al_{0.56-0.62}Fe_{0.24-0.32}Mg_{0.47-0.51}Si_{1.67-1.73}O_6$.

412 $_{1.73}O_6$. A single analysis of a Cpx inclusion in plagioclase shows the same composition as the

413 cores of the Cpx in the matrix.

414 By contrast, Cpx crystals in 18XC5 do not display any zoning and are characterized by X_{Mg}

415 and a Jd-component that range between 0.77-0.80 and 0.13-0.14 a.p.f.u., respectively. Their

416 stoichiometric formula corresponds to $Na_{0.13-0.14}Ca_{0.77-0.79}Al_{0.33-0.37}Fe_{0.17-0.19}Mg_{0.62-0.67}Si_{1.85-1.89}O_6$,

417 $_{1.89}O_6$, indicating that these pyroxenes are Al-poorer and Si- and Mg-richer than those

418 observed in 18XC1.

419 A lack of zoning is also observed in the Cpx from sample 18XC10. In this sample, pyroxenes

420 have a Jd-content between 0.13 and 0.16 a.p.f.u. and a X_{Mg} ranging between 0.70 and 0.73.

421 Additionally, Cpx display the lowest Al values (in a.p.f.u.) of all the analysed xenoliths, a

422 feature that is emphasized by the general stoichiometric formula, $Na_{0.14-0.17}Ca_{0.72-0.76}Al_{0.27-0.30}Fe_{0.24-0.28}Mg_{0.64-0.68}Si_{1.86-1.91}O_6$.

423 $_{0.30}Fe_{0.24-0.28}Mg_{0.64-0.68}Si_{1.86-1.91}O_6$.

424   For what concerns sample 18XC20, only a very weak zoning in Al can be observed in Cpx,

425   with rims being enriched compared to cores (see Fig. 5b). Crystal cores and rims have a Jd-

426   component between 0.17 and 0.20 a.p.f.u, while X_{Mg} is comprised between 0.63 and 0.67.

427   The stoichiometric formula for cores corresponds to $Na_{0.17-0.19}Ca_{0.72-0.74}Al_{0.35-0.37}Fe_{0.29}Mg_{0.53-}$

428    $_{0.57}Si_{1.86-1.88}O_6$, whereas that of the rims is $Na_{0.17-0.20}Ca_{0.72-0.74}Al_{0.37-0.41}Fe_{0.29-0.31}Mg_{0.52-0.55}Si_{1.83-}$

429    $_{1.86}O_6$.

430   Amphibole crystals from sample 18XC1 are not zoned, with Si = 5.71-5.99 a.p.f.u., Ca =

431   1.70-1.79 a.p.f.u., Na = 0.62-0.77 a.p.f.u. and X_{Mg} = 0.62-0.65 (Supplementary Table S5). In

432   general, the amphiboles in 18XC1 can be classified as ferroan-pargasite. Rim-core analyses

433   of a single amphibole grain in 18XC5 show that the crystal is pargasitic in composition and

434   has rims slightly depleted in Mg (3.04-3.08 a.p.f.u.) compared to the core (3.12-3.14 a.p.f.u.).

435   For what concerns the other elements, Si varies between 6.12 and 6.15 a.p.f.u., Ca and Na

436   between 1.60-1.64 and 0.77-0.81 a.p.f.u., respectively, while X_{Mg} is comprised between 0.75

437   and 0.76 for both core and rim. In sample 18XC10 amphiboles are also pargasitic and do not

438   display zoning, with Si = 6.10-6.16 a.p.f.u., Ca = 1.51-1.55 a.p.f.u., Na = 0.82-0.94 a.p.f.u.

439   and X_{Mg} = 0.67-0.70. In sample 18XC20 amphiboles from the matrix, as well as those

440   included in garnet and Cpx were measured. The amphiboles from the matrix have

441   composition ranging from ferroan-pargasite to pargasite, with Si = 5.83-6.14 a.p.f.u., Ca =

442   1.51-1.63 a.p.f.u., Na = 0.79-0.95 a.p.f.u. and X_{Mg} = 0.56-0.59 (Fig. 6a). On the other hand,

443   the amphibole inclusions measured in different garnet grains have a chemical composition

444   that ranges from cummingtonite (Si = 6.19-6.39 a.p.f.u., Ca = 1.19-1.22 a.p.f.u., Na = 0.44-

445   0.62 a.p.f.u., X_{Mg} = 0.58) to ferroan-pargasite (Si = 5.87-6.01 a.p.f.u., Ca = 1.65-1.66 a.p.f.u.,

446   Na = 0.67-0.72 a.p.f.u., X_{Mg} = 0.51-0.60). By contrast, the amphibole inclusions found in

447   different clinopyroxene crystals are more homogeneous, showing a ferroan-pargasitic

448   composition, with Si = 5.90-5.98 a.p.f.u., Ca = 1.60-1.63 a.p.f.u., Na = 0.93-0.95 a.p.f.u. and

449   X_{Mg} = 0.56-0.58.

450   The plagioclase crystals observed in 18XC1 are not zoned and have a X_{An} [X_{An} =

451   Ca/(Ca+Na+K)] that ranges between 0.48 and 0.55, corresponding to andesine-labradorite.

452   By contrast, a plagioclase vein within garnet displays a nearly pure anorthitic composition

453   (X_{An} = 0.92-0.98).

454   Plagioclase from sample 18XC10 is homogeneous and has a distinctive oligoclasic

455   composition (X_{An} = 0.25-0.27). On the other hand, some plagioclases in 18XC20 show a very

456   weak zoning (see Fig. 6b), with Ca-richer rims (X_{An} = 0.29-0.30) compared to cores (X_{An} =

457   0.27-0.28). A plagioclase pocket interstitial between two garnets shows different intergrowths

458   with compositions that vary between X_{An} = 0.29-0.30 and X_{An} = 0.51-0.55. Plagioclase

459   inclusions in garnets display a large variety of compositions (in different garnet crystals but

460   also within the same grain), with X_{An} between 0.28 and 0.61 (oligoclase to andesine).

461   Scapolite crystals measured in 18XC1 (Fig. 6c) and 18XC5 are characterized by high

462   concentrations in sulphur, with SO_3 that ranges between 3.1 and 5.4 wt.% and therefore can

463   be defined as silvialite. All the measured scapolites are not zoned, showing a meionite

464   component [Me% = (Ca+Mg+Fe^{2+}+Mn+Ti)/(Na+K+Ca+Mg+Fe^{2+}+Mn+Ti)·100] between 69

465   and 73.

466

467   **Major and trace element compositions of melts**

468   Glass was analysed mostly in melt inclusions, but also in veinlets that infiltrated garnets and

469   in interstitial films, the latter probably containing the host lava which entered the xenoliths

470   (see Supplementary Table S6). Overall, the analysed melts cover a SiO_2-range from 57.5

471   wt.% to 75.3 wt.%, forming distinct clusters for each type of xenolith in the TAS diagram (Le

472   Bas et al., 1986; Fig. 7a). Melts with the lowest silica contents are observed in sample 18XC1

473   (57.5 – 63.5 wt.%), which are followed, with increasing SiO_2, by analyses from samples

474   18XC20 (61.3 – 72.0 wt.%), 18XC5 (70.7 – 71.4 wt.%), and sample 18XC10 (69.1 – 75.2

475   wt.%). The average SiO_2 contents (on anhydrous basis and normalized to 100%) for the

476   analysed melt inclusions are: 60.9 ± 1.4 wt.% for 18XC1, 65.3 ± 1.1 wt.% for 18XC20, 71.2

477   ± 0.3 wt.% for 18XC5, and 72.4 ± 0.6 wt.% for 18XC10 (all errors expressed as 2 standard

478   error of the mean, 2 s.e.m., see also Table 1). According to the TAS classification, melts in

479   sample 18XC1 are dominantly andesitic in composition, those from sample 18XC20 are

480   trachytic to dacitic, while melts from 18XC5 and 18XC10 are mainly rhyolitic (Fig. 7a).

481   When plotted in the An-Or-Ab diagram (O'Connor, 1965; Supplementary Fig. S4) the

482   analysed melt inclusions for 18XC1 lie prevalently in the granodioritic field, those for 18XC5

483   and 18XC10 are dominantly trondhjemitic, while MI in 18XC20 range from tonalite to

484   trondhjemite in composition. The interstitial melts in 18XC10 and 18XC20 are tonalitic and

485   granitic, respectively, whereas the infiltrated melts in the same samples are mainly scattered

486   across the tonalitic and trondhjemitic fields (Supplementary Fig. S4). Moreover, most of the

487   melts observed in the xenoliths displays a peraluminous character (Fig. 7b). In Harker

488   diagrams (Fig. 8a-k) sample 18XC1 is characterized by a negative correlation with SiO_2 for

489   TiO_2 (although this correlation becomes positive for TiO_2 < 0.3 wt.%), FeO and MgO,

490   whereas Al_2O_3, Na_2O, K_2O, and P_2O_5 show a nearly constant correlation with increasing

491   silica. Moreover, some of the MI measured in sample 18XC1 have the highest concentrations

492   in CaO, FeO, and MgO. MI in sample 18XC20 are negatively correlated with SiO_2 for Al_2O_3,

493   whereas for CaO and Na_2O a negative trend is present, but less pronounced. The infiltrated

494   melt measured in 18XC20 shows a negative correlation with increasing silica for Al_2O_3, CaO,

495   MgO, and slightly also for P_2O_5, whereas for TiO_2, Na_2O and K_2O the trend remains

496   constant. MI analysed for sample 18XC10 show a strong negative correlation with SiO_2 for

497   Al_2O_3, while for FeO, MgO, and Na_2O the negative trend is less defined. All other elements

498   are highly scattered and no correlation with silica can be observed. The infiltrated melt

499   measured in 18XC10 shows a clear negative correlation for Al_2O_3, whereas the other oxides

500   display a large scattering. On the other hand, the interstitial melt in 18XC10 is characterized

501   by a negative trend for TiO_2, Al_2O_3, CaO, P_2O_5, and in a lesser extent also for FeO and MgO

502   vs. SiO_2, whereas for Na_2O and K_2O the trend is almost constant. Remarkable is the high

503   variability in P_2O_5 displayed by the interstitial melt, which was measured in two different

504   locations of a mm-sized melt pocket, with analyses between 0.34 and 0.64 wt.% P_2O_5 that

505   belong to the same location.

506   In the absence of a direct quantification of H_2O in the glasses, the EPMA analytical totals of

507   MI suggest that the melts within MI may have a moderate H_2O content of about 2.3 ± 0.8

508   wt.% (2 s.e.m.) in sample 18XC1, 1.0 ± 0.4 wt.% (2 s.e.m.) in sample 18XC10 and 2.7 ± 0.6

509   wt.% (2 s.e.m.) in sample 18XC20. The glass in the MI in scapolite from sample 18XC5 and

510   the interstitial melt in sample 18XC10 may be slightly more hydrous, with up to 4.5 wt.%

511   H_2O.

512   Trace elements vs. SiO_2 show a negative trend for Rb and U+Th in MI from sample 18XC20,

513   which display the highest concentrations for these elements, and a weak positive correlation

514   for Zr in both 18XC20 and 18XC10, with the latter sample showing the highest

515   concentrations (up to 152 μg/g). Another distinctive feature observed in 18XC10 is that the

516   interstitial melt has lower U+Th concentrations compared to the MI. Comparable low

517   concentrations in U+Th can be noticed also for a MI analysed in 18XC1, which by contrast

518   has Rb and Zr concentrations like 18XC20.

519   Trace elements normalized to the primitive mantle (McDonough & Sun, 1995) display very

520   similar patterns, with a strong enrichment in large ion lithophile elements (LILE), a marked

521   Nb-Ta anomaly, a strong positive anomaly for Pb and a weak to strong positive anomaly for

522   Sr (Fig. 9a-c). Analyses of the interstitial melt measured in sample 18XC10 show lower U

523 and K concentrations, a weaker Nb-Ta anomaly and a positive P anomaly compared to the

524 other melts.

525

526 **Geothermobarometry**

527 Pressure and temperature conditions were determined by conventional geothermobarometry

528 for all the investigated samples alongside with a detailed investigation by phase equilibria

529 modelling, intracrystalline geothermometry (Fe-Mg order-disorder on clinopyroxene) and

530 elastic geothermobarometry for sample 18XC10 (Fig. 10a-b), which displays a particularly

531 well-equilibrated mineral assemblage.

532 Conventional geothermobarometry was carried out using the thermometers of Nakamura

533 (2009) and Sudholz et al. (2022), which are based on Fe-Mg exchange between garnet and

534 clinopyroxene, and the barometer of Beyer et al. (2015). Uncertainty on temperature was

535 calculated by error propagation using the *Metas.UncLib* Python script (Zeier et al., 2012),

536 while for pressure we assumed the maximum error as reported in Beyer et al. (2015). In

537 general, the intersections of the geothermometers with the geobarometer give similar results

538 (see Table 2 and Supplementary Fig. S5). The highest temperatures and pressures are

539 observed for the rim analysis of a Grt-Cpx pair from sample 18XC1, with values up to 1480

540 °C and 3.0 GPa, while sample 18XC5 shows temperatures between 960 and 1030 °C and

541 pressures between 1.3 and 1.6 GPa. A similar range, within error, is also observed for

542 18XC10, whereas 18XC20 displays slightly higher values, with temperature and pressure that

543 range from 1100 °C to 1130 °C and 1.3 and 1.9 GPa, respectively.

544 For what concerns intracrystalline geothermometry, on the basis of the pyroxene chemical

545 analyses, the calibration reported in equation 4 by Brizi et al. (2000) has been adopted to

546 determine the closure temperature on seven pyroxene crystals of sample 18XC10. The

547 resulting temperatures range from 1050 to 1140 °C, with a calculated average at 1090 ± 30

548 °C (2 s.e.m.) (Fig. 10b and Supplementary Table S4).

549 Phase equilibria modelling for sample 18XC10 was performed starting from a bulk rock

550 composition (see caption to Fig. 10) determined combining the mineral proportions estimated

551 from an entire SEM compositional map (see Supplementary Fig. S2b) and the mineral

552 chemistry acquired by EPMA. Although the thin section shows two distinct zones (see

553 above), the mode of the entire thin section (54.3 vol.% garnet, 25.0 vol.% clinopyroxene,

554 18.0 vol.% plagioclase, 2.0 vol.% amphibole, 0.5 vol.% rutile and 0.2 vol.% apatite) was

555 used, since the chemical compositions of the minerals are the same in both zones.

556 Calculations indicates that the peak mineral assemblage observed in sample 18XC10 (Grt-

557 Cpx-Pl-Amp-Rt-melt) is predicted to be stable in a P-T field located at 1.5 – 1.8 GPa and 850

558 – 1080 °C (Fig. 10a). The low-T boundary of such field corresponds to the calculated solidus,

559 and quartz is predicted to be stable just below the solidus. Amphibole disappears at about

560 1050 °C in this pressure range. Calculated modal proportions of each mineral phase

561 (isomodes) reproduce the amounts of minerals present in 18XC10 (see Supplementary Fig.

562 S6). As an example, at 1000 °C and 1.7 GPa, the model predicts the following mineral

563 modes: 57.2 vol.% garnet, 25.5 vol.% clinopyroxene, 15.3 vol.% plagioclase, 0.9 vol.%

564 amphibole and 0.4 vol.% rutile, in agreement with the observed mineral mode. Conversely,

565 when compositional isopleths are plotted on the phase diagram (Supplementary Fig. S6) the

566 predicted compositions of phases in the Grt-Cpx-Pl-Amp-Rt-melt field do not completely

567 match the measured ones. In particular, modelled garnet composition is more calcic,

568 clinopyroxene is more magnesian, and plagioclase is more albitic. On the other hand, the

569 model shows a better fit for the almandine and pyrope components of garnet, as well for the

570 jadeite content in clinopyroxene.

571   Each sample displays a characteristic, relatively narrow, range of H_2O contents in the glasses

572   of MI. Along with the lack of decrepitation textures, such sample-specific melt H_2O contents

573   point against H_2O loss or gain from glass inclusions. Assuming that they represent the

574   original values, also the H_2O contents of MI inferred from the EPMA total closure can be

575   used to constrain the P-T conditions of their entrapment. In particular, at a given pressure,

576   they can provide the minimum temperature at which that melt may occur. Extrapolation to

577   higher pressures of the experiments on the haplogranite system (Holtz et al., 2001; Makhluf

578   et al., 2017) would suggest temperatures >1100 °C for sample 18XC10, >1050 °C for

579   samples 18XC1 and 18XC20, and ~950 °C for 18XC5, at a reference pressure of 1.5 GPa.

580   These temperatures vary as a function of pressure with a dependence of about 200°C/GPa in

581   the P-T region of interest (Makhluf et al., 2017).

582   Results from Raman measurements on zircon and quartz inclusions from sample 18XC10 are

583   shown in Fig. 10b and Fig. 11, and reported in the Supplementary Table S3.

584   The P_{inc} of quartz inclusions is the same in a 2σ uncertainty for inclusions both within the

585   same garnet and amongst different garnets. Zircon inclusions were found only within one

586   garnet but also show similar inclusion pressure within their uncertainties. Therefore, we

587   averaged the P_{inc} of the same inclusions from the same growth zone (least-squares weighted

588   average, using the uncertainty on P_{inc} as weighing factor) to calculate one representative

589   entrapment isomeke for quartz (average P_{inc} = 0.02 ± 0.05 GPa, 2 s.e.m.) and one for zircon

590   (average P_{inc} = 1.09 ± 0.03 GPa, 2 s.e.m.; Fig. 11). The average P_{inc} for zircons and quartz

591   suggest a P-T range of 1150 ± 30 °C (2 s.e.m.) and 1.9 ± 0.2 GPa (2 s.e.m.) (Fig. 10b). Such

592   P-T values for 18XC10 are consistent with those obtained from the other applied methods

593   (i.e., conventional geothermobarometry, phase equilibria and intracrystalline

594   geothermometry) and also with the peak metamorphic conditions suggested by Bloch et al.

595   (2017) for the Mercaderes arclogites.

596 **DISCUSSION**

597 **Petrographic constraints from microstructures**

598 The present research builds extensively on information provided by inclusions in the main

599 rock-forming minerals of the xenoliths, in particular by inclusions in garnet.

600 MI in crustal xenoliths are more common in volcanic rocks from extensional settings (e.g.,

601 the Pannonian Basin, Németh et al., 2021; the Neogene Volcanic Province of SE Spain,

602 Acosta-Vigil et al., 2007) than in continental arcs (e.g., Pamir, Chupin et al., 2006). At

603 Mercaderes, the occurrence of melt and quartz inclusions in clinopyroxene and garnet was

604 already reported by Weber et al. (2002) in two samples of garnet-pyroxene hornblendites.

605 From these observations the authors inferred that quartz should have been present at some

606 point in the initial rock assemblage, but they did not speculate further.

607 In the arclogite xenoliths of this study, MI occur in garnet from samples 18XC1, 18XC10 and

608 18XC20, whereas quartz inclusions in garnet are observed in samples 18XC5, 18XC10 and

609 18XC20. In sample 18XC10, where both inclusion types are most abundant (Fig. 3a,b;

610 Supplementary Fig. S1i), their classical "zonal arrangement" (Roedder, 1984) demonstrates

611 their primary origin, i.e., that the garnet grew in the presence of both quartz and melt. The

612 lack of quartz in the rest of the xenoliths outside garnet suggests that during or after garnet

613 growth quartz was totally consumed, remaining only as armoured inclusions in garnet.

614 During this process garnet also trapped rutile and zircon crystals.

615 Fresh or devitrified glass occurs in the xenoliths also along grain boundaries or in thin

616 layers/veinlets. The thinner films coating most grain boundaries (e.g., Fig. 2c) probably

617 represent reaction rims which formed during and after the entrainment of xenoliths in the host

618 lava. Similar features are common in lower crustal xenoliths both at Mercaderes and in other

619 regions (e.g., Hacker et al., 2005). The wider irregular veinlets that crosscut the xenoliths are

620 instead the result of infiltration of the host lava (e.g., Fig. 2a).

621 The former presence of melt in the xenoliths is also attested by diagnostic microstructures

622 such as plagioclase with crystal faces defining a subhedral shape (Sawyer, 2008; Holness et

623 al., 2011). These microstructures occur in samples 18XC1, 18XC10 and 18XC20 (e.g., Fig.

624 2b,g) and attest for crystallization of the plagioclase in patches and layers of former melt.

625 This process is compatible with both a cumulitic and a residual origin: in the former case the

626 melt would represent the intercumulus phase, in the latter an anatectic melt.

627 Melt inclusions often contain sub-micrometric nanolite crystals (Fig. 3h) that represent

628 daughter minerals from the cooling melt. A more detailed discussion on the nanolites can be

629 found in the supplementary Appendix.

630

631 **Comparison with MI from other tectonic settings**

632 Melt inclusions from Mercaderes were compared with MI from crustal xenoliths of other

633 tectonic settings (i.e., Ichinomegata arc, St. Kitts arc, Bohemian Massif, Neogene Volcanic

634 Province, and Bakony–Balaton Highland Volcanic Field) in order to put some constraints on

635 the formation of felsic melts in the lower crust.

636 MI observed in sample 18XC1 are low in silica and generally have high concentrations in

637 TiO_2, Al_2O_3, CaO, FeO and MgO indicating a more "intermediate" character compared to the

638 MI from the other xenoliths (Fig. 8a-k). Some MI from the St. Kitts arc (Melekhova et al.,

639 2017) and from the Bakony–Balaton Highland Volcanic Field (western Pannonian basin,

640 Hungary; Németh et al., 2021) have also similar low SiO_2 contents, but the other oxides do

641 not share similarities with the MI from Mercaderes. Melts analysed in sample 18XC20 partly

642 overlap the field displayed by the plagioclase-hosted MI from the Ichinomegata arc

643 (Yanagida et al., 2018) for TiO_2, Al_2O_3, Na_2O and K_2O at same SiO_2 contents, but are

644 enriched in FeO and MgO and slightly depleted in CaO and P_2O_5. The SiO_2-rich melts

645 observed in sample 18XC10 are clearly distinct from the MI observed in the Neogene

ORIGINAL UNEDITED MANUSCRIPT

646 Volcanic Province in Spain which were produced by anatexis of a metapelitic protolith

647 (Acosta-Vigil et al., 2007; Bartoli et al., 2016; Cesare et al., 2003; Ferrero et al., 2011), but

648 share many similarities with the MI from the Ichinomegata arc (in particular with the

649 magnetite-hosted MI), and from the granulites in SE Pamir (Chupin et al., 2006). The latter,

650 however, have a reverse K_2O/Na_2O ratio. Analogies with MI from the Bohemian Massif

651 (Borghini et al., 2018; Borghini, 2020; Ferrero et al., 2019) are displayed only for Al_2O_3,

652 FeO, MgO, Na_2O and P_2O_5. However, the MI from the Bohemian Massif show a strong

653 depletion in TiO_2 and CaO and a strong enrichment in K_2O compared to the melts measured

654 in the xenoliths from Mercaderes. For what concerns the MI measured in the scapolite

655 crystals of sample 18XC5, they are very similar to the melts from the Bohemian Massif,

656 although the latter are notably depleted in TiO_2 and enriched in K_2O.

657 The strong enrichment in LILE, the negative Nb-Ta and Ti anomalies, as well as the positive

658 Pb and Sr anomalies consistently displayed by the glasses from the Mercaderes xenoliths are

659 all features typical for subduction-related melts (Fig. 9a-c). The negative Nb-Ta anomalies

660 observed in MI and in the infiltrated melt suggest that rutile and/or ilmenite were part of the

661 partial melting residue or fractionated during crystallization. This is in agreement with the

662 mineral assemblage of the xenoliths, where rutile (sometimes rimmed by ilmenite, see

663 Supplementary Fig. S3) is commonly observed. The positive Sr anomaly of these melts may

664 derive from the partial melting of plagioclase. Sequestration of Nb, Ta and Ti in rutile or

665 ilmenite characterizes also the normalized patterns of the interstitial melt from sample

666 18XC10, which is interpreted to represent the host lava that percolated into the xenolith. The

667 interstitial melt also shows positive anomalies for Ba and Sr, as well as a weak to moderate

668 negative Eu anomaly $[Eu_N/(Sm_N \cdot Gd_N)^{1/2} = 0.39\text{-}0.89]$, with the latter that may indicate early

669 fractionation of plagioclase or retention of plagioclase in the source. Additionally, the

670   positive P anomaly of the interstitial melt also suggest that the host lava was generated from

671   the melting of a phosphorus-bearing phase (likely apatite) present in the source.

672   Trace element normalized patterns for the melts from Mercaderes are generally enriched

673   compared to MI in migmatitic paragneisses from the Himalaya (Bartoli et al, 2019), with the

674   latter also lacking a negative anomaly for Nb-Ta (Fig. 9b). By contrast, the MI from the

675   Bohemian Massif are strongly enriched in LILE (except for Ba) and Nb-Ta compared to

676   Mercaderes, which, on the other hand, perfectly overlap the pattern displayed by the MI from

677   the Bakony–Balaton Highland Volcanic Field. MI and infiltrated melt from the Mercaderes

678   xenoliths have mantle-normalized trace element patterns that generally lie between the upper

679   crust and lower crust compositions of Rudnick & Gao (2003) but show a slight enrichment in

680   Th-U and a strong depletion in Nb-Ta and Ti. Moreover, the interstitial melt measured in

681   sample 18XC10 displays a strong depletion in middle and heavy rare earth elements, as well

682   as in Ti and Y compared to the upper and lower crust.

683

684   **Comparison of MI with experimental melts and leucosomes in arcs**

685   Chemical compositions of melt inclusions from Mercaderes were compared with liquids

686   obtained from partial melting experiments of amphibolites between 1.0 and 1.6 GPa (Wolf &

687   Wyllie, 1994; Rapp & Watson, 1995; López & Castro, 2001) and with modelled melt

688   compositions for sample 18XC10, calculated from our phase equilibria modelling with

689   Perple_X (see Fig. 12). Additionally, leucosomes from exhumed arc roots, in particular from

690   the Fiordland arc (Daczko et al., 2001), the Kohistan arc (Garrido et al., 2006), the

691   Amalaoulaou arc (Berger et al., 2011) and the Bougmane arc (Triantafyllou et al. 2018) were

692   also used as references to evaluate the nature of the melts observed in the xenoliths from

693   Mercaderes (see Fig. 9c and Supplementary Fig. S7). In general, from Fig. 12 it is possible to

694   notice that MI from 18XC1 are different compared to the experimental melts, notably in their

695   TiO$_2$, Al$_2$O$_3$ and alkali contents. MI and infiltrated melts analysed in 18XC20 share some

696   similarities with the melts obtained by Wolf & Wyllie (1994) and Rapp & Watson (1995), but

697   are characterized by lower TiO$_2$ and higher K$_2$O contents. By contrast, the interstitial melt

698   from sample 18XC20 correlates with the compositions recovered from experiments only for

699   MgO and CaO. In a similar fashion, MI from sample 18XC5 systematically do not overlap

700   (except for TiO$_2$) the fields displayed by the anatectic experimental melts. Glasses from

701   18XC10 are comparable to the experimental compositions of Rapp & Watson (1995) at 1.6

702   GPa and ~1000 °C, although the first are slightly richer in CaO and MgO, and poorer in FeO

703   and Na$_2$O. Furthermore, Fig. 12 also shows that the melt compositions modelled with

704   Perple_X in the predicted stability field of 18XC10, i.e. at 900-1075 °C and 1.6-1.75 GPa, do

705   not fit with the measured melts. This discrepancy may rely on the fact that the

706   thermodynamic database and solution models used in Perple_X are calibrated only on few

707   experiments and bulk compositions at these P-T conditions.

708   Compared to leucosomes from exhumed arc roots, which have all been interpreted to result

709   from the partial melting of mafic lithologies (Daczko et al., 2001; Garrido et al., 2006; Berger

710   et al., 2011; Triantafyllou et al., 2018), glasses within the xenoliths from Mercaderes show

711   some differences, both in major and trace elements. In general, MI from 18XC1 have major

712   element compositions that do not correlate with the leucosomes (Supplementary Fig. S7),

713   suggesting that they may not have an anatectic origin. Some glasses from 18XC20 and

714   18XC10 have similar compositions as leucosomes from the Kohistan arc (although the latter

715   display trends with lower TiO$_2$ and K$_2$O, and higher CaO contents), while MI from sample

716   18XC5 display some analogies as leucosomes from the Bougmane arc, especially for Al$_2$O$_3$,

717   FeO and Na$_2$O (Supplementary Fig. S7).

718   MI and infiltrated melts within the garnet crystals of the xenoliths have primitive normalized

719   trace element patterns (Fig. 9c) that show some deviations compared to the normalized

720 patterns of the anatectic leucosomes from the Amalaoulaou, the Bougmane and the Fiordland

721 arcs. In particular, the glasses in the MI from the Mercaderes xenoliths are typically more

722 enriched in LILE, Pb, Hf and Zr than the leucosomes from these arcs. On the other hand,

723 leucosomes from the Kohistan paleo-arc are more similar to the patterns displayed by the

724 glasses from Mercaderes, but still show a depletion in Th, U and Hf compared to the latter

725 (Fig. 9c). The interstitial melt from sample 18XC10 has REE normalized patterns similar to

726 those observed for the leucosomes from the Kohistan and Amalaoulaou arc, but displays

727 higher Zr-Hf values compared to the leucosomes.

728 In general, the comparison of major and trace elements shows that MI and infiltrated melts

729 from samples 18XC10 and 18XC20 are more akin to melts obtained in partial melting

730 experiments of amphibolitic starting materials, and also to anatectic leucosomes from the

731 Kohistan and Amalaoulaou arc sections. MI from sample 18XC5 poorly correlate with

732 experimental melts, but have some similarities with the leucosomes from the Bougmane arc,

733 which have been interpreted to derive from disequilibrium melting of a mafic protolith

734 (Triantafyllou et al., 2018). By contrast, MI from sample 18XC1 have chemical compositions

735 that neither resemble those from partial melting experiments, nor natural anatectic

736 leucosomes, suggesting that sample 18XC1 may have a different origin.

737

738

739 **Origin of the studied arclogites**

740 The chemical composition of the melt entrapped in the primary MI, the latter indicative that

741 the host minerals were growing in the presence of a felsic melt, and a careful evaluation of

742 the microstructures displayed by the different xenoliths allow us to speculate about their

743 origin.

744 The melt within MI in garnet from samples 18XC10 is rhyolitic in the TAS classification and

745 mostly tonalitic-trondhjemitic in the An-Or-Ab diagram (Supplementary Fig. S4).

746 Experiments of partial melting of low-K metabasalts (Rapp & Watson, 1995) show that at 1.6

747 GPa Na-rich trondhjemitic to tonalitic liquids are produced by fluid-absent amphibole

748 melting in the temperature range 1000-1050°C. These low percentage (<10 vol.%) melts

749 coexist with a Grt-Cpx-Amp-Pl ± Qz ± Opx residue in which quartz, amphibole and

750 plagioclase are progressively consumed during heating. The Grt-Cpx-dominated mineralogy

751 of these experimental residues (Rapp & Watson, 1995, their figure 3) is therefore compatible

752 with the mineral assemblage observed in 18XC10. The same conclusion is also supported by

753 other experiments of fluid-absent melting of basaltic amphibolite at 1.0 GPa (Wolf & Wyllie,

754 1994), as well as at 1.5 and 2.0 GPa (Sen & Dunn, 1994). Hence, the experimental evidence

755 supports the interpretation that arclogitic xenoliths with felsic MI and quartz inclusions in

756 garnet are formed by low-degree partial melting of a (meta)basaltic source, a process that can

757 produce peritectic garnet and clinopyroxene with an anatectic trondhjemitic melt and justify

758 the entrapment of primary felsic MI in garnet. When talking about a (meta)basaltic source,

759 we envisage the rocks constituting the mafic lower crust in arc roots, which may range from

760 igneous textured gabbros, to their metamorphic equivalents dominated by amphibolites and

761 mafic granulites.

762 Thermodynamic modelling of basaltic compositions also corroborates these results, even

763 though these calculations predict lower temperatures for low degrees of anatexis (800-900

764 °C, Palin et al., 2016; Ducea et al., 2021b). Such thermodynamic simulations were performed

765 using wet basaltic bulk compositions. Also our modelling of the residual composition of

766 sample 18XC10 predicts a solidus at 850 °C at 1.6-1.8 GPa, and the onset of melting through

767 quartz consumption. All this evidence is in accordance with the general assumption that these

768   types of restitic arclogites in the subarc lower crust derive from the partial melting of

769   underplated (meta)basalts (Lee & Anderson, 2015; Bowman et al., 2021).

770   Conversely, the silica-rich composition of MI is incompatible with a cumulitic origin of

771   xenoliths like 18XC10, since garnets obtained in high pressure crystallization experiments

772   will not be able to entrap melts with comparable high SiO_2 as in sample 18XC10. Indeed,

773   cumulitic garnet clinopyroxenites are predicted to form primarily by crystallization of

774   basaltic magmas (Green & Ringwood, 1967a,b; Lee & Anderson, 2015 and references

775   therein). Although garnet and clinopyroxene have been observed as liquidus phases of more

776   silicic melts (Carroll and Wyllie, 1990; Alonso-Perez at al., 2009), the andesitic compositions

777   used in these experiments contain >10 wt.% less silica than the MI from sample 18XC10. In

778   addition, none of the above experiments could explain the presence of quartz, found as

779   primary inclusions along with MI, in a growing garnet that eventually could form a cumulate.

780   Sample 18XC20 is a Hbl+Grt+Pl±Cpx xenolith characterized by MI with a dacitic/tonalitic

781   compositions (Fig. 7a and Supplementary Fig. S4) and the presence of quartz inclusions in

782   the cores of the garnets. Xenoliths consisting of Hbl+Grt+Pl+Cpx have been also observed in

783   early Miocene high-silica andesites and dacites from the Northland Peninsula (New Zealand).

784   These xenoliths have been interpreted to be cognate, i.e., directly crystallized form the host

785   calc-alkaline lavas (Day et al., 1992). Further experimental studies on H_2O-bearing dacites

786   (3-5 wt.% H_2O) from the Northland Peninsula have shown that at P > 1.3 GPa Grt and Cpx

787   can be liquidus phases, and that Qz and Amp (ferroan pargasite to edenitic hornblende)

788   appear together, while Cpx disappears, at T < 920-900 °C (Green, 1992).Although we do not

789   disregard the possibility that 18XC20 might have a cumulitic origin after fractional

790   crystallization of a dacitic melt, the presence of quartz inclusions associated to primary melt

791   inclusions solely in the garnet cores, and not in the matrix of the xenolith, points more

792 towards a restitic formation and the conclusions derived from 18XC10 seem to be valid also

793 for 18XC20.

794 The melt entrapped in the MI found in scapolite from sample 18XC5 is rhyolitic (Fig. 7a) and

795 fall well within the trondhjemitic field of the An-Or-Ab diagram (Supplementary Fig. S4).

796 MI in scapolite have been also noticed in granulitic xenoliths from diatremes in south-eastern

797 Pamir (Tajikistan), which were interpreted to be the result of incongruent partial melting of

798 lower crustal lithologies at P > 1.3 GPa and T ~ 1000 °C (Chupin et al., 2006). Similar P-T

799 conditions have been determined by geothermobarometry also for sample 18XC5.

800 Additionally, considering the rhyolitic composition of the MI and the presence of Qz

801 inclusions in the garnets, it can be inferred that 18XC5 may have also been formed after

802 incongruent partial melting of a metabasaltic lithology.

803 Sample 18XC1 shows significant differences with respect to the other three arclogites: a

804 greater abundance of plagioclase and amphibole, the lack of quartz inclusions in garnet, and

805 the (trachy)andesitic composition of MI in garnet. Even though straightforward textures are

806 not observed, these features could be more compatible with a cumulate origin rather than

807 with a restitic one. The mineral assemblage may in fact be produced by the crystallization of

808 an andesitic melt with moderate H_2O contents at P > 1 GPa (Alonso-Perez et al., 2009), and

809 the 18XC1 arclogite could represent a cumulate after this process. This interpretation is also

810 corroborated by the less evolved composition of the glass measured in the MI, which is not

811 consistent with melts from partial melting experiments and natural anatectic leucosomes (see

812 above). The H_2O content in the MI of about 2.0 ± 1.0 wt.% (s.e.m.), for sample 18XC1 would

813 passively increase during crystallization of garnet and clinopyroxene, and be partly used for

814 the later crystallization of amphibole. The density for sample 18XC1, calculated from its

815 modal assemblage, is 3.23 g/cm^3.

816 Combining the textural, chemical and thermobarometric constraints provided in this study,

817 we propose that the arclogite xenoliths that contain primary MI and quartz inclusions in

818 garnet represent restites after the re-melting of a mafic, Qz-bearing protolith. This conclusion

819 is supported in particular by sample 18XC10, where the genetic constraints are best evident.

820 The re-melting of a mafic crust produced a Grt-Cpx-rich residue with minor plagioclase and

821 amphibole, and progressively consumed quartz that must have been present in the protolith

822 and is preserved only as inclusions in the cores of garnet. In order to produce a silica-rich

823 trondhjemitic anatectic melt, the degree of melting was low (Rapp & Watson, 1995). Similar

824 conclusions seem to be valid also for samples 18XC5 and 18XC20.

825 Therefore, we provide evidence for the presence of both cumulitic and restitic arclogites in

826 the lower portion of the active Colombian volcanic arc.

827 The arclogites equilibrated at temperature of 960-1150 °C and pressure of ~1.6 – 2.0 GPa,

828 corresponding to a depth of 60-75 km in the arc root assuming a crustal density of 2.7 g/cm^3.

829 The thermobarometric estimates obtained for our samples fit with the P-T array defined by

830 the crustal xenoliths from Mercaderes studied by Bloch et al. (2017), that should represent the

831 present-day geotherm in the arc region. Our results are also consistent with new geophysical

832 investigations, that infer a crustal thickness of 64.5-72.5 km for the Colombian volcanic arc

833 (Avellaneda-Jiménez & Monsalve, 2022). The anomalously high P-T conditions calculated

834 for rim (3.0 GPa, 1400 °C) and core (2.0 GPa, 1260 °C) of a Grt-Cpx pair in sample 18XC1

835 may indicate that the two minerals were not in chemical equilibrium and therefore these

836 results have been excluded for further discussions on the equilibration conditions of this

837 xenolith.

838 Sample 18XC10 is a typical low MgO (10.2 wt.%), low X_{Mg} (0.58) pyroxenite in the

839 distinction of Lee & Anderson (2015). Its density, calculated from its chemical and modal

840 composition, is >3.4 g/cm^3 as expected from low MgO arclogites (Lee & Anderson, 2015;

841 Ducea et al., 2021a,b) and confirms that this rock is negatively buoyant relative to the upper

842 mantle and has the potential for foundering/delamination from the arc roots (Bloch et a.,

843 2017).

844 Unlike other xenoliths at Mercaderes (Weber et al., 2002), sample 18XC10 shows very little

845 evidence of reaction rims and growth of secondary amphibole at grain boundaries. In

846 addition, both garnet and clinopyroxene grains are compositionally homogeneous. These

847 feature, also observed in earlier studies (Weber et al., 2002; Bloch et al., 2017) indicate that

848 part of the xenoliths, including 18XC10, were in P-T equilibrium in the region of residence at

849 the time of entrapment in the host magma, and their assemblages were not affected by the

850 ascent toward the surface or to shallower depths prior to eruption.

851

852 **Potentials of elastic thermobarometry**

853 Pressure-temperature conditions for arclogites from the literature typically describe a wide

854 field between 700-950 °C and 1.0-3.0 GPa (e.g., California; Ducea & Saleeby, 1996; central

855 Arizona, Rautela et al., 2020). Arclogites from Mercaderes suggest instead a much higher

856 equilibration temperature of about 1100-1200 °C, which has been linked to crustal foundering

857 (Bloch et al., 2017).

858 Classical geothermobarometric techniques coupled with thermodynamic modelling for the

859 mineral assemblage of sample 18XC10 suggest the rock formed from partial melting at P-T

860 conditions of ~1050 ± 100 °C (2 s.e.m.) and 1.5-1.8 GPa. These conditions agree with the Fe-

861 Mg order-disorder thermometry on clinopyroxene, which records an average closure

862 temperature of 1090 ± 30 °C (2 s.e.m.) and are therefore consistent with the partial melting of

863 a lower arc (meta)basaltic rock at H_2O-undersaturated conditions. Moreover, our results fall

864 along the geothermal gradient defined by Bloch et al. (2017) for the Mercaderes area (Fig.

865 10b).

866 Elastic geothermobarometry of quartz and zircon inclusion in garnet suggest higher P-T

867 conditions of 1150 ± 30°C (2 s.e.m.) and 1.9 ± 0.2 GPa (2 s.e.m.). Results of elastic

868 geobarometry can provide pressure and temperature conditions of inclusion entrapment

869 within a mineral host. However, examples of non-elastic processes in inclusion-host systems

870 are numerous (e.g., Campomenosi et al., 2021). Also, post-entrapment shape maturation of

871 quartz within garnet might also affect the elastic behaviour of the system (Cesare et al.,

872 2021). Recent experimental investigations on zircon inclusion in garnet (Campomenosi et al.

873 2022) showed that non-elastic re-equilibration of host-inclusion system is P-T path- rather

874 than temperature-dependent. Such mechanical resetting occurs when a zircon in garnet, after

875 entrapment, is heated to temperatures greater than those of entrapment, or is decompressed

876 isothermally (Campomenosi et al., 2021;2022). The zircon-in-garnet host-inclusion system

877 thus records the maximum temperature at the lowest pressure reached by the system.

878 Therefore, we propose that zircon inclusions in sample 18XC10 were entrapped, along with

879 quartz and melt inclusions, at ~1050 °C, 1.5-1.8 GPa, and were then plastically reset at 1150

880 °C and 1.9 ± 0.2 (2 s.e.m.) GPa. Quartz-in-garnet geobarometry is consistent with both the P-

881 T conditions suggested by thermodynamic modelling and by zircon-in-garnet geobarometry.

882 Shape maturation mechanisms of quartz at high temperature which lead to inclusion faceting

883 (see Fig. 3k) might be related to non-elastic reset (Cesare et al., 2021), but clear experimental

884 proofs are still lacking. Since it is unknown whether quartz undergoes a non-elastic reset

885 similarly to zircon, it is unclear whether this isomeke records the entrapment conditions

886 during partial melting or the plastic reset at higher temperature.

887 Sample 18XC10 might therefore support the hypothesis of crustal foundering in the

888 Mercaderes-Río Mayo area, because by looking at the absolute values of its possible P-T

889 path, one can notice that the sample displays a prograde heating path from 1050 °C and 1.6

890 GPa to 1150 °C and 1.9 GPa. However, we also recognize that, due to the high error on the

891 Fe-Mg exchange geothermobarometers, the conclusion that sample 18XC10 shows

892 foundering at the mineral grain scale should be taken with care.

893

894 **Tectonic implications**

895 The Mercaderes area is a rare, if not the unique, example where both residues from partial

896 melting of metabasalts and cumulates from the high-pressure crystallization of

897 basaltic/andesitic mantle-derived liquids along an active Cordilleran margin can be directly

898 observed. This corroborates the idea that these two (apparently) antithetic rock-forming

899 processes can occur in a single setting such as the lower arc crust (Bowman et al. 2021),

900 especially in mature arcs, where the crustal section may exceed 50 km in thickness.

901 The interplay between lower crust anatexis and crystallization of mantle-derived melts, both

902 leading to the formation of dense mafic arclogites, has important implications for the

903 formation and geochemical evolution of volcanic arcs. A first possible consequence is that

904 the dacitic to rhyolitic melts produced during the partial melting of metabasaltic protoliths

905 may interact and hybridize the primitive basalts derived by the partial melting of the mantle

906 (see Fig. 13). Such a process, might justify part of the crustal signature observed in many

907 granitic batholiths and which has been typically related to the crustal assimilation of the

908 surrounding country rock (e.g., DePaolo, 1981; Ague & Brimhall, 1987). Secondly, the

909 formation of arclogites (both cumulates or restites) denser than the underlying lithospheric

910 mantle implies a physical instability of the arc root (Lee & Anderson, 2015; Bowman et al.

911 2021; Ducea et al. 2021a,b), with arclogites that undergo foundering into the mantle and

912 eventually may delaminate (complete detachment from the base of the arc). Density sorting in

913 lower arc roots has been suggested to be one of the major mechanisms that drives arc

914 magmas towards high silica contents and consequently towards a bulk arc crust more akin to

915 an andesitic continental crust (e.g., Jagoutz & Schmidt, 2013; Jagoutz & Behn, 2013; Ducea

916   et al. 2021b). The density calculated for sample 18XC10 is 4-7 % higher than that of the

917   lithospheric mantle (assuming a density of 3.30 ± 0.05 g/cm^3), consistent with the values

918   estimated by Bloch et al. (2017) for some Grt-clinopyroxenites from the same region.

919   Therefore, it seems plausible that, as suggested by Bloch et al. (2017), the lower continental

920   crust between the Colombian Western and Central Cordilleras is currently subjected to

921   foundering into the lithospheric mantle. However, Bowman et al. (2021) have shown that the

922   process of foundering is strongly dependent on the amount of the melt in equilibrium with the

923   residues that is retained by the system. For melt volumes lower than 10-18 vol.%, it is

924   suggested that the arclogites are prone to founder, while at higher melt volumes they are

925   stabilized in the arc root. Furthermore, it is also inferred that the arclogites may be partially

926   re-melted, while sinking into the mantle, favouring its re-fertilization (Bowman et al. 2021;

927   Ducea et al. 2021b). The melting behaviour of the foundering arclogites will ultimately

928   depend on the regional geotherm and hotter geotherms will produce larger amounts of melt

929   than colder ones. As a consequence, and in analogy to what proposed by Bowman et al.

930   (2021), the tendency to sink for this crustal blob will be inversely proportional to the amount

931   of melt present in the system (since this melt has a much lower density), with 'drained' blobs

932   that will have the highest tendency to continue along their sinking trajectory. This hypothesis

933   was tested by monitoring the supra-solidus density evolution of sample 18XC10 along three

934   geotherms (500 °C/GPa, 600 °C/GPa and 640 °C/GPa) that intersect and bound the stability

935   field of the rock estimated by Perple_X, and along the geotherm of 720 °C/GPa determined

936   by Bloch et al. (2017) for the Mercaderes area (see Fig. 10a). Within the P-T field calculated

937   by Perple_X it is possible to notice that the total density of the system (residue + melt)

938   decreases with increasing degree of melting, while the density of the residue increases (see

939   Supplementary Fig. S8 and Supplementary Table S7). As expected, the largest variations in

940   density, both for the total system and the residue, are displayed along the hotter geotherms.

941   This implies that the effective sinking of a partially molten rock similar to sample 18XC10

942   depends on the amount of melt that is retained in it, with the consequence that at high melt

943   volumes the blob may reach a neutral buoyancy with the surrounding mantle and pond. On

944   the other hand, if some of the melt is released during the descent of the blob, then the density

945   is predominantly governed by the density of the solid residue, leading to a negative buoyancy

946   of the crustal blob.

947

948   **CONCLUSIONS**

949   The roots of volcanic continental and oceanic arcs are important interfaces where major

950   exchanges of mass between mantle and crust occur. Arc roots are characterized by a dual

951   nature, in which high pressure crystallization and partial melting play a fundamental role in

952   the formation and evolution of the bulk arc crust. Cumulates and restites resulting from these

953   two distinct processes have similar mineral assemblages, thus making any unambiguous

954   inference on their origin very difficult. Additionally, field evidence for re-melting of mafic

955   orthogneisses and/or amphibolites within volcanic arcs has been reported to be limited and

956   equivocal (Jagoutz & Klein, 2018). Nevertheless, in our study we could demonstrate that a

957   careful petrographical and microstructural investigation of mineral and melt inclusions and

958   their geochemical characterization may help in the discrimination of the two endmembers. In

959   particular, the concomitant presence of quartz inclusions closely associated to MI in the

960   garnet cores of the investigated xenoliths has been interpreted to be diagnostic for restitic

961   arclogites. Although we cannot, and do not want to, speculate on the relative importance of

962   cumulus versus re-melting processes for the origin of arclogites, our study provides the first

963   field-based evidence that some arclogite xenoliths from Mercaderes-Río Mayo are residues

964   after partial melting of a metabasaltic crust, suggesting also that the occurrence of magmatic

965   cumulates and anatectic restites may be concomitant, especially in mature arcs, where the arc

966 root has a considerable thickness. It is also proposed that the thick root of mature arcs is a

967 more favourable zone for melt hybridization and delamination of dense residues compared to

968 the root of thin arcs.

969

980

981 **REFERENCES**

982 Acosta-Vigil, A., London, D., Morgan, G. B. & Dewers, T. A. (2003). Solubility of excess

983   alumina in hydrous granitic melts in equilibrium with peraluminous minerals at 700–

984   800 °C and 200 MPa, and applications of the aluminum saturation index.

985 *Contributions to Mineralogy and Petrology* **146**, 100–119.

986 Acosta-Vigil, A., Cesare, B., London, D. & Morgan, G. B. (2007). Microstructures and

987   composition of melt inclusions in a crustal anatectic environment, represented by

988   metapelitic enclaves within El Hoyazo dacites, SE Spain. *Chemical Geology* **237**,

989 450- 465.

990 Ague, J.J. & Brimhall, G.H. (1987). Granites of the batholiths of California: Products of local

991   assimilation and regional-scale crustal contamination. *Geology* **15**, 63-66.

992 Alonso-Perez, R., Müntener, O. & Ulmer, P. (2009). Igneous garnet and amphibole

993   fractionation in the roots of island arcs: experimental constraints on andesitic liquids.

994   *Contributions to Mineralogy and Petrology* **157**, 541-558.

995 Angel, R.J., Mazzucchelli, M.L., Alvaro, M., Nimis, P. & Nestola, F. (2014). Geobarometry

996   from host-inclusion systems: The role of elastic relaxation. *American Mineralogist* **99**,

997   2146-2149.

998 Angel, R.J., Alvaro, M., Miletich, R. & Nestola, F. (2017a). A simple and generalised P–T–

999   V EoS for continuous phase transitions, implemented in EosFit and applied to quartz.

1000   *Contributions to Mineralogy and Petrology* **172**, 1-15.

1001 Angel, R.J., Mazzucchelli, M.L., Alvaro, M. & Nestola, F. (2017b). EosFit-Pinc: A simple

1002   GUI for host-inclusion elastic thermobarometry. *American Mineralogist* **102**, 1957-

1003   1960.

1004 Angel, R.J., Murri, M., Mihailova, B. & Alvaro, M. (2019). Stress, strain and Raman shifts.

1005   *Zeitschrift für Kristallographie-Crystalline Materials* **234**, 129-140.

1006 Angel, R.J., Gilio, M., Mazzucchelli, M. & Alvaro, M. (2022). Garnet EoS: a critical review

1007   and synthesis. *Contributions to Mineralogy and Petrology* **177**, 1-22.

1008 Avellaneda-Jiménez, D.S. & Monsalve, G. (2022). Arclogite nature of the Colombian Andes

1009   magmatic arc root: A receiver-function approach. *Tectonophysics* **836**, 1-10.

1010 Bartoli, O., Acosta-Vigil, A., Ferrero, S. & Cesare, B. (2016). Granitoid magmas preserved as

1011   melt inclusions in high-grade metamorphic rock. *American Mineralogist* **101**, 1543-

1012   1559.

1013 Bartoli, O., Acosta-Vigil, A., Cesare, B., Remusat, L., Gonzalez-Cano, A., Wälle, M.,

1014   Tajčmanová L. & Langone, A. (2019). Geochemistry of Eocene-Early Oligocene low-

1015   temperature crustal melts from Greater Himalayan Sequence (Nepal): a nanogranitoid

1016   perspective. *Contribution to Mineralogy and Petrology* **174**, 1-18.

1017   Behrens, H. & Jantos, N. (2001). The effect of anhydrous composition on water solubility in

1018   granitic melts. *American Mineralogist* **86**, 14–20.

1019   Berger, J., Caby, R., Liégeois, J.P., Mercier, J.C.C. & Demaiffe, D. (2011). Deep inside a

1020   neoproterozoic intra-oceanic arc: growth, differentiation and exhumation of the

1021   Amalaoulaou complex (Gourma, Mali). *Contributions to Mineralogy and Petrology*

1022   **162**, 773-796.

1023   Beyer, C., Frost, D.J. & Miyajima, N. (2015). Experimental calibration of a garnet–

1024   clinopyroxene geobarometer for mantle eclogites. *Contributions to Mineralogy and*

1025   *Petrology* **169**, 1-21.

1026   Binvignat, F.A.P., Malcherek, T., Angel, R.J., Paulmann, C., Schlüter, J. & Mihailova, B.

1027   (2018). Radiation-damaged zircon under high pressures. *Physics and Chemistry of*

1028   *Minerals* **45**, 981-993.

1029   Bloch, E., Ibañez-Mejia, M., Murray, K., Vervoort, J. & Müntener, O. (2017). Recent crustal

1030   foundering in the Northern Volcanic Zone of the Andean arc: Petrological insights from

1031   the roots of a modern subduction zone. *Earth and Planetary Science Letters* **476**, 47-58.

1032   Borghini, A., Ferrero, S., Wunder, B., Laurent, O., O'Brien, P. J. & Ziemann, M. A. (2018).

1033   Granitoid melt inclusions in orogenic peridotite and the origin of garnet

1034   clinopyroxenite. *Geology* **46**, 1007-1010.

1035   Borghini, A. (2020). Melt inclusions in mafic rocks as witnesses of metasomatism in the

1036   Bohemian Massif. PhD diss., Universität Potsdam, 2020, 1-205.

1037   Bowman, E.E., Ducea, M.N. & Triantafyllou, A. (2021). Arclogites in the subarc lower crust:

1038   effects of crystallization, partial melting, and retained melt on the foundering ability of

1039   residual roots. *Journal of Petrology* **62**, 1-22.

1040   Brizi, E., Molin, G. and Zanazzi, P.F. (2000). Experimental study of intracrystalline Fe^{2+}-Mg

1041   exchange in three augite crystals: Effect of composition on geothermometric

1042   calibration. *American Mineralogist* **85**, 1375-1382.

1043   Burg, J. P. (2011). The Asia–Kohistan–India collision: review and discussion. In: *Arc-*

1044   *continent collision* (pp. 279-309). Springer, Berlin, Heidelberg.

1045   Campomenosi, N., Rubatto, D., Hermann, J., Mihailova, B., Scambelluri, M. & Alvaro, M.

1046   (2020). Establishing a protocol for the selection of zircon inclusions in garnet for

1047   Raman thermobarometry. *American Mineralogist: Journal of Earth and Planetary*

1048   *Materials* **105**, 992-1001.

1049   Campomenosi, N., Scambelluri, M., Angel, R.J., Hermann, J., Mazzucchelli, M.L.,

1050   Mihailova, B., Piccoli, F. & Alvaro, M. (2021). Using the elastic properties of zircon-

1051   garnet host-inclusion pairs for thermobarometry of the ultrahigh-pressure Dora-Maira

1052   whiteschists: problems and perspectives. *Contributions to Mineralogy and Petrology*

1053   **176**, 1-17.

1054   Campomenosi, N., Angel, R.J., Alvaro, M. & Mihailova, B. (2022). Resetting of zircon

1055   inclusions in garnet: Implications for elastic thermobarometry. *Geology*, 1-5.

1056   Carroll, M.R. & Wyllie, P.J. (1990). The system tonalite-H_2O at 15 kbar and the genesis of

1057   calc-alkaline magmas. *American Mineralogist* **75**, 345-357

1058   Cesare, B., Marchesi, C., Hermann, J. & Gómez-Pugnaire, M. T. (2003). Primary melt

1059   inclusions in andalusite from anatectic graphitic metapelites: implications for the

1060   position of the Al_2SiO_5 triple point. *Geology* **31**, 573-576.

1061   Cesare, B., Parisatto, M., Mancini, L., Peruzzo, L., Franceschi, M., Tacchetto, T., Reddy, S.,

1062   Spiess, R., Nestola, F. & Marone, F. (2021). Mineral inclusions are not immutable:

1063   Evidence of post-entrapment thermally-induced shape change of quartz in garnet. *Earth*

1064   *and Planetary Science Letters* **555**, 116708.

ORIGINAL UNEDITED MANUSCRIPT

1065 Chupin, V.P., Kuz'min, D.V. & Madyukov, I.A. (2006). Melt inclusions in minerals of

1066   scapolite-bearing granulite (lower crustal xenoliths from diatremes of the Pamirs).

1067   *Doklady earth sciences* **407A**, 507-511.

1068 Connolly, J.A. (2005). Computation of phase equilibria by linear programming: a tool for

1069   geodynamic modeling and its application to subduction zone decarbonation. *Earth and*

1070   *Planetary Science Letters* **236**, 524-541.

1071 Connolly, J.A.D. (2009). The geodynamic equation of state: what and how. *Geochemistry,*

1072   *geophysics, geosystems* **10**, 1-19.

1073 Daczko, N.R., Clarke, G.L. & Klepeis, K.A. (2001). Transformation of two-pyroxene

1074   hornblende granulite to garnet granulite involving simultaneous melting and fracturing

1075   of the lower crust, Fiordland, New Zealand. *Journal of Metamorphic Geology* **19**, 549-

1076   562.

1077 Day, R.A., Green, T.H. & Smith, I.E.M. (1992). The origin and significance of garnet

1078   phenocrysts and garnet-bearing xenoliths in Miocene calc-alkaline volcanics from

1079   Northland, New Zealand. *Journal of Petrology* **33**, 125-161.

1080 DeBari, S. M. & Greene, A. R. (2011). Vertical stratification of composition, density, and

1081   inferred magmatic processes in exposed arc crustal sections. In: *Arc-continent collision*

1082   (pp. 121-144). Springer, Berlin, Heidelberg.

1083 DePaolo, D.J. (1981). Trace element and isotopic effects of combined wallrock assimilation

1084   and fractional crystallization. *Earth and planetary science letters* **53**, 189-202.

1085 Domeneghetti, M.C., Fioretti, A.M., Cámara, F., McCammon, C. & Alvaro, M. (2013).

1086   Thermal history of nakhlites: A comparison between MIL 03346 and its terrestrial

1087   analogue Theo's flow. *Geochimica et Cosmochimica Acta* **121**, 571-581.

Ducea, M.N. & Saleeby, J.B. (1996). Buoyancy sources for a large, unrooted mountain range, the Sierra Nevada, California: Evidence from xenolith thermobarometry. *Journal of Geophysical Research: Solid Earth* **101**, 8229-8244.

Ducea, M. N., Otamendi, J. E., Bergantz, G. W., Jianu, D., & Petrescu, L. (2015). The origin and petrologic evolution of the Ordovician Famatinian-Puna arc. *Geological Society of America Memoirs* **212**, 125-138.

Ducea, M. N., Chapman, A. D., Bowman, E. & Triantafyllou, A. (2021a). Arclogites and their role in continental evolution; part 1: Background, locations, petrography, geochemistry, chronology and thermobarometry. *Earth-Science Reviews* **214**, 103375.

Ducea, M.N., Chapman, A.D., Bowman, E. & Balica, C. (2021b). Arclogites and their role in continental evolution; part 2: relationship to batholiths and volcanoes, density and foundering, remelting and long-term storage in the mantle. *Earth-Science Reviews* **214**, 103476.

Ehlers, A.M., Zaffiro, G., Angel, R.J., Boffa-Ballaran, T., Carpenter, M.A., Alvaro, M. & Ross, N.L. (2022). Thermoelastic properties of zircon: Implications for geothermobarometry. *American Mineralogist: Journal of Earth and Planetary Materials* **107**, 74-81.

Ferrero, S., Bodnar, R. J., Cesare, B. & Viti, C. (2011). Re-equilibration of primary fluid inclusions in peritectic garnet from metapelitic enclaves, El Hoyazo, Spain. *Lithos* **124**, 117-131.

Ferrero, S., O'Brien, P. J., Borghini, A., Wunder, B., Wälle, M., Günter, C. & Ziemann, M. A. (2019). A treasure chest full of nanogranitoids: an archive to investigate crustal melting in the Bohemian Massif. *Geological Society, London, Special Publications* **478**, 13-38.

1112   Ganguly, J. (1982). Mg-Fe order-disorder in ferromagnesian silicates: II. Thermodynamics,

1113   kinetics, and geological applications. *Journal of Environmental Sciences (China)*

1114   *English Ed*, 58-99.

1115   Garrido, C. J., Bodinier, J. L., Burg, J. P., Zeilinger, G., Hussain, S. S., Dawood, H., Nawaz

1116   Chaudhry, M. & Gervilla, F. (2006). Petrogenesis of mafic garnet granulite in the lower

1117   crust of the Kohistan paleo-arc complex (Northern Pakistan): implications for intra-

1118   crustal differentiation of island arcs and generation of continental crust. *Journal of*

1119   *Petrology* **47**, 1873-1914.

1120   Green, D.H. & Ringwood, A.E. (1967a). The genesis of basaltic magmas. *Contributions to*

1121   *Mineralogy and Petrology* **15**, 103-190.

1122   Green, D.H. & Ringwood, A.E. (1967b). An experimental investigation of the gabbro to

1123   eclogite transformation and its petrological applications. *Geochimica et Cosmochimica*

1124   *Acta* **31**, 767-833.

1125   Green, E.C.R., White, R.W., Diener, J.F.A., Powell, R., Holland, T.J.B. & Palin, R.M.

1126   (2016). Activity–composition relations for the calculation of partial melting equilibria

1127   in metabasic rocks. *Journal of metamorphic Geology* **34**, 845-869.

1128   Green, T.H. (1992). Experimental phase equilibrium studies of garnet-bearing I-type

1129   volcanics and high-level intrusives from Northland, New Zealand. *Earth and*

1130   *Environmental Science Transactions of the Royal Society of Edinburgh* **83**, 429-438.

1131   Greene, A. R., DeBari, S. M., Kelemen, P. B., Blusztajn, J. & Clift, P. D. (2006). A detailed

1132   geochemical study of island arc crust: the Talkeetna Arc section, south–central Alaska.

1133   *Journal of Petrology* **47**, 1051-1093.

1134   Hacker, B., Luffi, P., Lutkov, V., Minaev, V., Ratschbacher, L., Plank, T., Ducea, M., Patiño-

1135   Douce, A., McWilliams, M. & Metcalf, J. (2005). Near-ultrahigh pressure processing of

1136   continental crust: Miocene crustal xenoliths from the Pamir. *Journal of Petrology* **46**,

1137   1661-1687.

1138   Hacker, B. R., Kelemen, P. B. & Behn, M. D. (2011). Differentiation of the continental crust

1139   by relamination. *Earth and Planetary Science Letters* **307**, 501-516.

1140   Hacker, B. R., Kelemen, P. B. & Behn, M. D. (2015). Continental lower crust. *Annual*

1141   *Review of Earth and Planetary Sciences* **43**, 167-205.

1142   Holland, T. & Powell, R. (2003). Activity–composition relations for phases in petrological

1143   calculations: an asymmetric multicomponent formulation. *Contributions to Mineralogy*

1144   *and Petrology* **145**, 492-501.

1145   Holness, M.B., Cesare, B. & Sawyer, E.W. (2011). Melted rocks under the microscope:

1146   microstructures and their interpretation. *Elements* **7**, 247-252.

1147   Holtz, F., Johannes, W., Tamic, N. & Behrens, H. (2001). Maximum and minimum water

1148   contents of granitic melts generated in the crust: a reevaluation and implications. *Lithos*

1149   **56**, 1-14.

1150   Ingamells, C.O., 1978. Analyzed minerals for electron microprobe standards. *Geostandards*

1151   *Newsletter* **2**, 115.

1152   Jagoutz, O. & Schmidt, M. W. (2012). The formation and bulk composition of modern

1153   juvenile continental crust: the Kohistan arc. *Chemical Geology* **298–299**, 79–96.

1154   Jagoutz, O. & Behn, M. D. (2013). Foundering of lower island-arc crust as an explanation for

1155   the origin of the continental Moho. *Nature* **504**, 131-134.

1156   Jagoutz, O. & Schmidt, M. W. (2013). The composition of the foundered complement to the

1157   continental crust and a re-evaluation of fluxes in arcs. *Earth and Planetary Science*

1158   *Letters* **371**, 177-190.

1159   Jagoutz, O. & Kelemen, P. B. (2015). Role of arc processes in the formation of continental

1160   crust. *Annual Review of Earth and Planetary Sciences* **43**, 363-404.

1161   Jagoutz, O. & Klein, B. (2018). On the importance of crystallization-differentiation for the

1162   generation of SiO_2-rich melts and the compositional build-up of arc (and continental)

1163   crust. *American Journal of Science* **318**, 29-63.

1164   Jarosewich, E., Nelen, J.A. & Norberg, J.A. (1980). Reference samples for electron

1165   microprobe analysis. *Geostandards Newsletter* **4**, 43-47.

1166   Jarosewich, E. (2002). Smithsonian microbeam standards. *Journal of research of the*

1167   *National Institute of Standards and Technology* **107**, 681-685.

1168   Kelemen, P. B., Hanghøj, K. & Greene, A. R. (2014). One View of the Geochemistry of

1169   Subduction-Related Magmatic Arcs, with an Emphasis on Primitive Andesite and

1170   Lower Crust. In: Holland, H. D. & Turekian, K. K. (eds) *Treatise on Geochemistry*,

1171   Vol. 3, 2nd edn. Amsterdam: Elsevier, 749-806.

1172   Kelemen, P. B. & Behn, M. D. (2016). Formation of lower continental crust by relamination

1173   of buoyant arc lavas and plutons. *Nature Geoscience* **9**, 197-205.

1174   Klein, B. Z. & Jagoutz, O. (2021). Construction of a trans-crustal magma system: building

1175   the Bear Valley Intrusive Suite, southern Sierra Nevada, California. *Earth and*

1176   *Planetary Science Letters* **553**, 116624.

1177   Kuzmany, H. (2009). Solid-state spectroscopy: an introduction. Berlin: springer, pp. 554.

1178   Le Bas, M. J., Le Maitre, R. W., Streckeisen, A. & Zanettin, A. (1986). A chemical

1179   classification of volcanic rocks based on the total alkali-silica diagram. *Journal of*

1180   *Petrology* **27**, 745-750.

1181   Lee, C.T.A., Cheng, X. & Horodyskyj, U. (2006). The development and refinement of

1182   continental arcs by primary basaltic magmatism, garnet pyroxenite accumulation,

1183   basaltic recharge and delamination: insights from the Sierra Nevada, California.

1184   *Contributions to Mineralogy and Petrology* **151**, 222-242.

1185 Lee, C. T. A. & Anderson, D. L. (2015). Continental crust formation at arcs, the arclogite

1186 "delamination" cycle, and one origin for fertile melting anomalies in the mantle.

1187 *Science Bulletin* **60**, 1141-1156.

1188 López, S. & Castro, A. (2001). Determination of the fluid–absent solidus and supersolidus

1189 phase relationships of MORB-derived amphibolites in the range 4–14 kbar. *American*

1190 *Mineralogist* **86**, 1396-1403.

1191 Makhluf, A.R., Newton, R.C. & Manning, C.E. (2017). Experimental determination of

1192 liquidus H_2O contents of haplogranite at deep-crustal conditions. *Contributions to*

1193 *Mineralogy and Petrology* **172**, 1-18.

1194 Mazzucchelli, M.L., Burnley, P., Angel, R.J., Morganti, S., Domeneghetti, M.C., Nestola, F.

1195 & Alvaro, M. (2018). Elastic geothermobarometry: Corrections for the geometry of the

1196 host-inclusion system. *Geology* **46**, 231-234.

1197 Mazzucchelli, M.L., Angel, R.J. & Alvaro, M. (2021). EntraPT: an online platform for elastic

1198 geothermobarometry. *American Mineralogist: Journal of Earth and Planetary*

1199 *Materials* **106**, 830-837.

1200 McDonough, W. F. & Sun, S. S. (1995). The composition of the Earth. *Chemical Geology*

1201 **120**, 223-253.

1202 Melekhova, E., Blundy, J., Martin, R., Arculus, R., & Pichavant, M. (2017). Petrological and

1203 experimental evidence for differentiation of water-rich magmas beneath St. Kitts,

1204 Lesser Antilles. *Contributions to Mineralogy and Petrology* **172**, 1-32.

1205 Morgan, G. B. & London, D. (2005). Effect of current density on the electron microprobe

1206 analysis of alkali aluminosilicate glasses. *American Mineralogist* **90**, 1131–1138.

1207 Murcia, L. A. & Cepeda, H. (1991). Mapa Geológico de Colombia, Plancha 410 La Unión,

1208 Memoria Explicativa. INGEOMINAS, Bogotá, 1-22.

1209   Murri, M., Mazzucchelli, M.L., Campomenosi, N., Korsakov, A.V., Prencipe, M., Mihailova,

1210   B.D., Scambelluri, M., Angel, R.J. & Alvaro, M. (2018a). Raman elastic geobarometry

1211   for anisotropic mineral inclusions. *American Mineralogist: Journal of Earth and*

1212   *Planetary Materials* **103**, 1869-1872.

1213   Murri, M., Cámara, F., Adam, J., Domeneghetti, M.C. & Alvaro, M. (2018b). Intracrystalline

1214   "geothermometry" assessed on clino and orthopyroxene bearing synthetic rocks.

1215   *Geochimica et Cosmochimica Acta* **227**, 133-142.

1216   Murri, M., Domeneghetti, M.C., Fioretti, A.M., Nestola, F., Vetere, F., Perugini, D., Pisello,

1217   A., Faccenda, M. & Alvaro, M. (2019). Cooling history and emplacement of a

1218   pyroxenitic lava as proxy for understanding Martian lava flows. *Scientific reports* **9**, 1-

1219   7.

1220   Nakamura, D. (2009). A new formulation of garnet–clinopyroxene geothermometer based on

1221   accumulation and statistical analysis of a large experimental data set. *Journal of*

1222   *Metamorphic Geology* **27**, 495-508.

1223   Németh, B., Török, K., Bali, E., Zajacz, Z., Fodor, L. & Szabó, C. (2021). Melt-rock

1224   interaction in the lower crust based on silicate melt inclusions in mafic garnet granulite

1225   xenoliths, Bakony-Balaton Highland Volcanic Field (Hungary). *Geologica Carpathica*

1226   **72**, 232-252.

1227   O'Connor, J. T. (1965). A classification for quartz-rich igneous rocks based on feldspar

1228   ratios. *United States Geological Survey Professional Paper* **525-B**, 79-84.

1229   Otamendi, J. E., Ducea, M. N., & Bergantz, G. W. (2012). Geological, petrological and

1230   geochemical evidence for progressive construction of an arc crustal section, Sierra de

1231   Valle Fertil, Famatinian Arc, Argentina. *Journal of Petrology* **53**, 761-800.

1232   Özkan, H., Cartz, L. & Jamieson, J.C. (1974). Elastic constants of nonmetamict zirconium

1233   silicate. *Journal of Applied Physics* **45**, 556-562.

1234 Palin, R.M., White, R.W., Green, E.C., Diener, J.F., Powell, R. & Holland, T.J. (2016). High-

1235   grade metamorphism and partial melting of basic and intermediate rocks. *Journal of*

1236   *Metamorphic Geology* **34**, 871-892.

1237 Paton, C., Hellstrom, J., Paul, B., Woodhead, J. & Hergt, J. (2011). Iolite: Freeware for the

1238   visualisation and processing of mass spectrometric data. *Journal of Analytical Atomic*

1239   *Spectrometry* **26**, 2508–2518.

1240 Petrelli, M., Laeger, K., & Perugini, D. (2016a). High spatial resolution trace element

1241   determination of geological samples by laser ablation quadrupole plasma mass

1242   spectrometry: implications for glass analysis in volcanic products. *Geosciences Journal*

1243   **20**, 851–863. https://doi.org/10.1007/s12303-016-0007-z

1244 Petrelli, M., Morgavi, D., Vetere, F., & Perugini, D. (2016b). Elemental imaging and petro-

1245   volcanological applications of an improved Laser Ablation Inductively Coupled

1246   Quadrupole Plasma Mass Spectrometry. *Periodico di Mineralogia* **85**, 25–39.

1247   https://doi.org/10.2451/2015PM0465

1248 Poveda, E., Monsalve, G. & Vargas, C.A. (2015). Receiver functions and crustal structure of

1249   the northwestern Andean region, Colombia. *Journal of Geophysical Research: Solid*

1250   *Earth* **120**, 2408-2425.

1251 Rapp, R.P. & Watson, E.B. (1995). Dehydration melting of metabasalt at 8–32 kbar:

1252   implications for continental growth and crust-mantle recycling. *Journal of Petrology*

1253   **36**, 891-931.

1254 Rautela, O., Chapman, A.D., Shields, J.E., Ducea, M.N., Lee, C.T., Jiang, H. & Saleeby, J.

1255   (2020). In search for the missing arc root of the Southern California Batholith: PTt

1256   evolution of upper mantle xenoliths of the Colorado Plateau Transition Zone. *Earth and*

1257   *Planetary Science Letters* **547**, 1-13.

1258   Rodríguez-Vargas, A., Koester, E., Mallmann, G., Conceição, R. V., Kawashita, K. & Weber,

1259   M. B. I. (2005). Mantle diversity beneath the Colombian Andes, northern volcanic

1260   zone: Constraints from Sr and Nd Isotopes. *Lithos* **82**, 471-484.

1261   Roedder, E. (1984). Volume 12: fluid inclusions. *Reviews in mineralogy* **12**, Mineralogical

1262   Society of America, Washington, DC 1-646.

1263   Rosenfeld, J.L. & Chase, A.B. (1961). Pressure and temperature of crystallization from

1264   elastic effects around solid inclusions in minerals? *American Journal of Science* **259**,

1265   519-541.

1266   Rudnick, R. L. (1995). Making continental crust. *Nature* **378**, 571-578.

1267   Rudnick, R. L. & Gao, S. (2003). Composition of the continental crust. In: Holland, H. D. &

1268   Turekian, K. K. (eds) *Treatise on Geochemistry*, Vol. 3, 1st edn. Amsterdam: Elsevier,

1269   1-64.

1270   Saleeby, J.B. (1990). Progress in Tectonic and Petrogenetic Studies in an Exposed Cross-

1271   Section of Young (~100 Ma) Continental Crust, Southern Sierra Nevada, California. In:

1272   Salisbury, M.H., Fountain, D.M. (eds) *Exposed Cross-Sections of the Continental*

1273   *Crust*. NATO ASI Series, vol 317. Springer, Dordrecht, 137-158.

1274   Sawyer, E. W. (2008). Atlas of migmatites. The Canadian Mineralogist Special Publication 9.

1275   Quebec: Mineralogical Association of Canada; Ottawa: NRC Research Press.

1276   Schmidt, M. & Poli, S. (2013). Devolatilization during subduction. In: Holland, H. D. &

1277   Turekian, K. K. (eds) *Treatise on Geochemistry*, Vol. 4, 2nd edn. Amsterdam: Elsevier,

1278   669-701.

1279   Sen, C. & Dunn, T. (1994). Dehydration melting of a basaltic composition amphibolite at 1.5

1280   and 2.0 GPa: implications for the origin of adakites. *Contributions to Mineralogy and*

1281   *Petrology* **117**, 394-409.

1282 Sheldrick, G.M. (2008). A short history of SHELX. *Acta Crystallographica Section A:*

1283   *Foundations of Crystallography* **64**, 112-122.

1284 Stangarone, C., Angel, R.J., Prencipe, M., Campomenosi, N., Mihailova, B. & Alvaro, M.

1285   (2019). Measurement of strains in zircon inclusions by Raman spectroscopy. *European*

1286   *Journal of Mineralogy* **31**, 685-694.

1287 Sudholz, Z.J., Green, D.H., Yaxley, G.M. & Jaques, A.L. (2022). Mantle geothermometry:

1288   experimental evaluation and recalibration of Fe–Mg geothermometers for garnet-

1289   clinopyroxene and garnet-orthopyroxene in peridotite, pyroxenite and eclogite systems.

1290   *Contributions to Mineralogy and Petrology* **177**, 1-19.

1291 Syracuse, E.M., Maceira, M., Prieto, G.A., Zhang, H. & Ammon, C.J. (2016). Multiple plates

1292   subducting beneath Colombia, as illuminated by seismicity and velocity from the joint

1293   inversion of seismic and gravity data. *Earth and Planetary Science Letters* **444**, 139-

1294   149.

1295 Taboada, A., Rivera, L.A., Fuenzalida, A., Cisternas, A., Philip, H., Bijwaard, H., Olaya, J. &

1296   Rivera, C. (2000). Geodynamics of the northern Andes: Subductions and

1297   intracontinental deformation (Colombia). *Tectonics* **19**, 787-813.

1298 Tatsumi, Y. (2000). Continental crust formation by crustal delamination in subduction zones

1299   and complementary accumulation of the enriched mantle I component in the mantle.

1300   *Geochemistry, Geophysics, Geosystems* **1**, 1-17.

1301 Taylor, S. R. & McLennan, S. M. (1995). The geochemical evolution of the continental crust.

1302   *Review of Geophysics* **33**, 241–265.

1303 Triantafyllou, A., Berger, J., Baele, J.M., Bruguier, O., Diot, H., Ennih, N., Monnier, C.,

1304   Plissart, G., Vandycke, S. & Watlet, A. (2018). Intra-oceanic arc growth driven by

1305   magmatic and tectonic processes recorded in the Neoproterozoic Bougmane arc

1306   complex (Anti-Atlas, Morocco). *Precambrian Research* **304**, 39-63.

1307   Wang, J., Mao, Z., Jiang, F. & Duffy, T.S. (2015). Elasticity of single-crystal quartz to 10

1308   GPa. *Physics and Chemistry of Minerals* **42**, 203-212.

1309   Weber, M. B. I. (1998). The Mercaderes-Río Mayo xenoliths, Colombia: Their bearing on

1310   mantle and crustal processes in the Northern Andes. PhD diss., University of Leicester,

1311   1998, 1-295.

1312   Weber, M. B., Tarney, J., Kempton, P. D. & Kent, R. W. (2002). Crustal make-up of the

1313   northern Andes: evidence based on deep crustal xenolith suites, Mercaderes, SW

1314   Colombia. *Tectonophysics* **345**, 49-82.

1315   White, R.W., Powell, R., Holland, T.J.B. & Worley, B.A. (2000). The effect of TiO_2 and

1316 Fe_2O_3 on metapelitic assemblages at greenschist and amphibolite facies conditions:

1317   mineral equilibria calculations in the system K_2O-FeO-MgO-Al_2O_3-SiO_2-H_2O-TiO_2-

1318 Fe_2O_3. *Journal of Metamorphic Geology* **18**, 497-511.

1319   White, R.W., Powell, R. & Clarke, G.L. (2002). The interpretation of reaction textures in Fe-

1320   rich metapelitic granulites of the Musgrave Block, central Australia: constraints from

1321   mineral equilibria calculations in the system K_2O–FeO–MgO–Al_2O_3–SiO_2–H_2O–TiO_2–

1322 Fe_2O_3. *Journal of metamorphic Geology* **20**, 41-55.

1323   White, R.W., Powell, R., Holland, T.J.B., Johnson, T.E. & Green, E.C.R. (2014). New

1324   mineral activity–composition relations for thermodynamic calculations in metapelitic

1325   systems. *Journal of Metamorphic Geology* **32**, 261-286.

1326   Whitney, D.L. & Evans, B.W. (2010). Abbreviations for names of rock-forming minerals.

1327   *American mineralogist* **95**, 185-187.

1328   Wolf, M.B. & Wyllie, P.J. (1994). Dehydration-melting of amphibolite at 10 kbar: the effects

1329   of temperature and time. *Contributions to Mineralogy and Petrology* **115**, 369-383.

1330   Yanagida, Y., Nakamura, M., Yasuda, A., Kuritani, T., Nakagawa, M. & Yoshida, T. (2018).

1331   Differentiation of a hydrous arc magma recorded in melt inclusions in deep crustal

1332   cumulate xenoliths from Ichinomegata Maar, NE Japan. *Geochemistry, Geophysics,*

1333   *Geosystems* **19**, 838-864.

1334   Zeier, M., Hoffmann, J. & Wollensack, M. (2012). Metas.UncLib—A measurement

1335   uncertainty calculator for advanced problems. *Metrologia* **49**, 809-815.

1336

1337

1338

1339

1340

1341

1342

1343

1344

1345

1346

1347

1348

1349

1350

1351

1352

1353

1354

1355

1356

1357 Table 1: Average chemical compositions of the analysed glasses. Errors are expressed as two

1358 standard error of the mean (2 s.e.m.).

	Melt inclusions								Infiltrated melts				Interstitial melt	
	18XC1 (wt.%)	2 s.e.m.	18XC5 (wt.%)	2 s.e.m.	18XC10 (wt.%)	2 s.e.m.	18XC20 (wt.%)	2 s.e.m.	18XC20 (wt.%)	2 s.e.m.	18XC10 (wt.%)	2 s.e.m.	18XC10 (wt.%)	2 s.e.m.
SiO_2	60.87	1.43	71.21	0.33	72.39	0.62	65.34	1.09	67.41	2.07	72.33	0.95	72.49	1.09
TiO_2	0.38	0.13	0.46	0.04	0.36	0.03	0.25	0.07	0.20	0.03	0.40	0.04	0.33	0.11
Al_2O_3	20.09	0.33	17.33	0.14	14.99	0.41	18.40	0.75	16.27	0.98	14.98	0.60	14.74	0.50
FeO	4.66	1.39	0.36	0.09	2.39	0.31	3.86	0.45	5.25	0.70	2.32	0.51	2.99	0.20
MnO	0.18	0.06	-	-	0.10	0.05	0.18	0.03	0.15	0.06	0.09	0.04	0.13	0.04
MgO	1.18	0.46	0.21	-	0.73	0.12	1.11	0.15	1.31	0.18	0.77	0.20	0.63	0.06
CaO	6.01	0.83	0.78	0.07	2.29	0.24	3.73	0.33	3.30	0.52	2.56	0.26	3.49	0.27
Na_2O	3.84	0.31	6.80	0.27	4.64	0.36	5.03	0.42	4.33	0.77	4.36	0.35	3.88	0.21
K_2O	2.73	0.12	2.83	0.18	2.14	0.20	2.09	0.14	1.77	0.07	2.20	0.21	1.00	0.04
P_2O_5	0.12	0.02	0.18	0.04	0.12	0.01	0.14	0.02	0.10	0.02	0.15	0.02	0.35	0.15
Total anhydrous	100.00	-	100.00	-	100.00	-	100.00	-	100.00	-	100.00	-	100.00	-
Total EPMA	97.68	0.80	95.54	0.71	99.00	0.40	97.32	0.64	98.56	0.50	99.24	0.16	96.45	1.21
Na_2O+K_2O	6.57	0.31	9.63	0.23	6.78	0.30	7.12	0.45	6.10	0.74	6.55	0.33	4.88	0.22
$[Al_2O_3/(Na_2O+K_2O)]_{molar}$	2.18	0.11	1.22	0.02	1.52	0.05	1.78	0.10	1.86	0.36	1.58	0.07	1.98	0.13
$[Al_2O_3/(CaO+Na_2O+K_2O)]_{molar}$	1.00	0.05	1.11	0.03	1.07	0.03	1.08	0.05	1.09	0.11	1.06	0.02	1.07	0.03
$[K_2O/Na_2O+K_2O]_{molar}$ x 100	32.08	2.10	21.52	1.57	23.64	2.38	21.99	1.77	21.92	4.62	25.15	2.70	14.55	0.67
Na_2O+K_2O-CaO	0.56	1.03	8.85	0.18	4.49	0.42	3.39	0.48	2.80	0.98	3.99	0.44	1.39	0.37

1359

1360

ORIGINAL UNEDITED MANUSCRIPT

1361 Table 2: Conventional geothermobarometry. Errors on pressure and temperature are

1362 expressed as two standard error of the mean (2 s.e.m.).

	Nakamura (2009)		Beyer et al. (2015)		Sudholz et al. (2022)		Beyer et al. (2015)	
	T (°C)	2 s.e.m.	P (GPa)	2 s.e.m.	T (°C)	2 s.e.m.	P (GPa)	2 s.e.m.
18XC1								
18XC1 Grt-Cpx rim 1	1477	60	3.00	0.4	1399	26	2.77	0.4
18XC1 Grt-Cpx core 1	1264	127	2.14	0.4	1210	107	1.99	0.4
18XC5								
18XC5 Grt-Cpx rim 1	992	27	1.30	0.4	1008	24	1.34	0.4
18XC5 Grt-Cpx core 1	966	29	1.40	0.4	977	24	1.43	0.4
18XC5 Grt-Cpx rim 2	1021	63	1.48	0.4	1033	56	1.51	0.4
18XC5 Grt-Cpx core 2	960	39	1.54	0.4	972	31	1.58	0.4
18XC5 Grt-Cpx rim 3	1028	44	1.53	0.4	1034	40	1.54	0.4
18XC5 Grt-Cpx core 3	963	50	1.38	0.4	978	45	1.42	0.4
18XC10								
18XC10 Grt-Cpx rim 1	1021	85	1.30	0.4	1079	80	1.44	0.4
18XC10 Grt-Cpx core 1	1034	114	1.68	0.4	1083	109	1.82	0.4
18XC20								
18XC20 Grt-Cpx rim 1	1119	54	1.82	0.4	1129	51	1.85	0.4
18XC20 Grt-Cpx rim 2	1105	76	1.75	0.4	1120	74	1.79	0.4
18XC20 Grt-Cpx rim 3	1111	94	1.86	0.4	1126	91	1.91	0.4

1363

1364

1365

1366

1367

1368

1369

1370

1371

1372 **LIST FIGURE CAPTIONS MAIN TEXT**

1373

1374 **Fig. 1.** Tectonic map of the Mercaderes area (modified after Weber et al. 2002 and

1375 Rodríguez-Vargas et al. 2005). Coordinates are given according to WGS84.

1376

1377 **Fig. 2**. Main petrographic features of the studied arclogite xenoliths. (a) Network of fractures

1378 filled with partly crystallized melt (detail in inset). Sample 18XC1, plane polarized light

1379 (PPL). (b) Plagioclase with planar crystal faces (arrows). Sample 18XC1, crossed polarizers

1380 (XPL) and lambda plate (λ). (c) Evidence of pervasive reaction along all grain boundaries.

1381 Sample 18XC5, PPL. (d) Quartz inclusions in garnet. Sample 18XC5, PPL (left) and XPL, λ

1382 (right). (e) Well equilibrated granoblastic texture of sample 18XC10. PPL. (f) Abundant

1383 primary quartz inclusions at the core of garnet. Sample 18XC10. PPL. (g) Plagioclase with

1384 euhedral crystal faces (arrows). Sample 18XC20, XPL. (h) Quartz inclusions in garnet,

1385 suggestive of *necking-down* processes. Sample 18XC20, PPL (left) and XPL, λ (right).

1386

1387 **Fig. 3**. Main microstructures of inclusions in rock-forming minerals of the studied arclogite

1388 xenoliths. See text for further details. Inclusions are hosted in garnet except (i) and (j), hosted

1389 in plagioclase and rutile, respectively. All micrographs taken in PPL mode, except (f, bottom)

1390 taken under XPL, and (h) and (j), taken under backscattered electron imaging. (a) "Zonal

1391 arrangement" of primary inclusions of glass (red arrow), rutile (blue arrow) and quartz. (b)

1392 "Zonal arrangement" of primary inclusions of quartz, rutile (blue arrows) and glass. The red

1393 arrow points at an elongate quartz inclusion suggestive of *necking-down* processes (c-e)

1394 Examples of MI with negative crystal shape and one or more shrinkage bubbles. (f) Elongate

1395 MI with evidence of *necking-down*, multiple shrinkage bubbles, and one trapped crystal of

1396 quartz (red arrow on bottom view). (g) Examples of dark brown glass in MI from sample

1397   18XC20. (h) Nanolites in the glass of a MI in sample 18XC1. Close-up in inset. (i) Primary

1398   MI in plagioclase from sample 18XC1. (j) Primary MI in rutile from sample 18XC1. Detail in

1399   inset, also showing exsolution textures. (k) Faceted inclusions of quartz (red arrows) trapped

1400   in garnet.

1401

1402   **Fig. 4.** Representative garnet profiles (rim to rim) for the Mercaderes xenoliths. $X_{Grs} =$

1403 $Ca/(Ca+Fe^{2+}+Mg+Mn)$, $X_{Alm} = Fe^{2+}/(Ca+Fe^{2+}+Mg+Mn)$, $X_{Prp} = Mg/(Ca+Fe^{2+}+Mg+Mn)$ and

1404 $X_{Sps} = Mn/(Ca+Fe^{2+}+Mg+Mn)$. Uncertainties on analyses are smaller than the symbol size.

1405

1406

1407   **Fig. 5.** Representative clinopyroxene profiles (rim to rim) for the Mercaderes xenoliths.

1408   Cations given in atoms per formula units (a.p.f.u.). $X_{Mg} = Mg/(Mg+Fe^{TOT})$ and therefore

1409   dimensionless. Uncertainties on analyses are smaller than the symbol size.

1410

1411   **Fig. 6.** Representative profiles for amphibole (a), plagioclase (b) and scapolite (c) for the

1412   Mercaderes xenoliths. Cations given in atoms per formula units (a.p.f.u.). Ratios are defined

1413   as following: $X_{Mg} = Mg/(Mg+Fe^{TOT})$, $X_{An} = Ca/(Ca+Na+K)$, $X_{Ab} = Na/(Ca+Na+K)$, $X_{Or} =$

1414 $K/(Ca+Na+K)$ and $X_{Me} = (Ca+Mg+Fe^{2+}+Mn+Ti)/(Na+K+Ca+Mg+Fe^{2+}+Mn+Ti)$ are all

1415   dimensionless. The profiles for amphibole and plagioclase are rim to rim, whereas the profile

1416   for scapolite is core to rim. Uncertainties on analyses are smaller than the symbol size.

1417

1418   **Fig. 7.** Chemical classification of the glasses analysed in the Mercaderes xenoliths

1419   (normalized to 100% on anhydrous basis). (a) TAS diagram. (b) Aluminium saturation index

1420   versus alkalinity index. Errors on analyses are reported as 2s.

1421

1422   **Fig. 8.** (a-k) Harker diagrams for the analysed glasses. Reference analyses for the

1423   Ichinomegata arc are from Yanagida et al. (2018); for the Bohemian Massif from Borghini et

1424   al. (2018), Borghini (2020) and Ferrero et al. (2019); for the Neogene Volcanic Province

1425   (NVP) from Acosta-Vigil et al. (2007), Bartoli et al. (2016), Cesare et al. (2003) and Ferrero

1426   et al. (2011); for the St. Kitts arc from Melekhova et al. (2017); for the Bakony–Balaton

1427   Highland Volcanic Field (BBHVF) from Németh et al. (2021) and from south-eastern Pamir

1428   (Chupin et al., 2006). All analyses normalized to 100% on anhydrous basis. Errors on

1429   analyses are reported as 2s.

1430

1431

1432   **Fig. 9.** Normalized trace element patterns. (a) Melt inclusions (MI), infiltrated and interstitial

1433   melt from the Mercaderes xenoliths. (b) Comparison with MI from Himalaya (Bartoli et al.,

1434   2019), Bohemian Massif (Borghini et al. 2018; Ferrero et al., 2019) and the Bakony–Balaton

1435   Highland Volcanic Field (Németh et al., 2021). (c) Comparison with anatectic leucosomes

1436   from the Kohistan arc (Garrido et al., 2006), the Amalaoulaou arc (Berger et al., 2011), the

1437   Bougmane arc (Triantafyllou et al. 2018) and from the Fiordland arc (Daczko et al., 2001).

1438   Error bars are expressed as 2 standard error of the mean.

1439

1440   **Fig. 10.** Geothemobarometry for sample 18XC10. (a) Phase equilibria modelling with

1441   Perple_X using the following bulk rock composition: SiO_2 = 46.61 wt.%, Al_2O_3 = 17.61

1442   wt.%, MgO = 10.19 wt.%, FeO = 13.11 wt.%, MnO = 0.27 wt.%, CaO = 9.79 wt.%, Na_2O =

1443   1.79 wt.%, K_2O = 0.07 wt.%, TiO_2 = 0.53 wt.% and H_2O = 0.04 wt.%. The bulk rock

1444   composition was determined combining the mineral proportions estimated from a SEM

1445   compositional map and the mineral chemistry acquired by EPMA. The ellipse highlights the

1446   stability field of the xenolith. Different geothermal gradients are also displayed. Points on the

1447   geothermal gradients represent P-T conditions above the solidus at which the density of the

1448   system (residue + melt) was investigated with Perple_X. (b) Summary of all the

1449   geothermobarometric methods applied on sample 18XC10. The geothermal gradient

1450   calculated by Bloch et al. (2017) is also shown.

1451

1452   **Fig. 11.** Strains and inclusion pressure of quartz and zircon inclusions in garnet. (a) Quartz.

1453   (b) Zircon. The hydrostatic stress lines of quartz and zircon (solid blue lines) and those of

1454   equal inclusion pressure (dash-dot lines in black) were produced by converting the strain into

1455   stress with the available elastic tensor for quartz (Wang et al., 2015) and zircon (Özkan et al.,

1456   1974), disregarding stiffening or softening effects with pressure. The uncertainty on P_{inc} was

1457   obtained by propagating the uncertainty on strain (the variance-covariance matrix) through

1458   the procedure described in Mazzucchelli et al. (2021). Error bars are expressed as 1s.

1459

1460   **Fig. 12**. (a-g) Harker diagrams for the analysed glasses compared with experimental liquids

1461   obtained by partial melting of amphibolite starting materials and melts calculated with

1462   Perple_X for sample 18XC10. All analyses normalized to 100% on anhydrous basis. Errors

1463   on analyses are reported as 2s.

1464

1465   **Fig. 13.** Schematic cartoon (not to scale) showing the formation of cumulitic and restitic

1466   arclogites in the lower arc crust and the development of hybrid melts.

1467

1468

1469

1470

1471

1472   **Fig. 1.**

1473
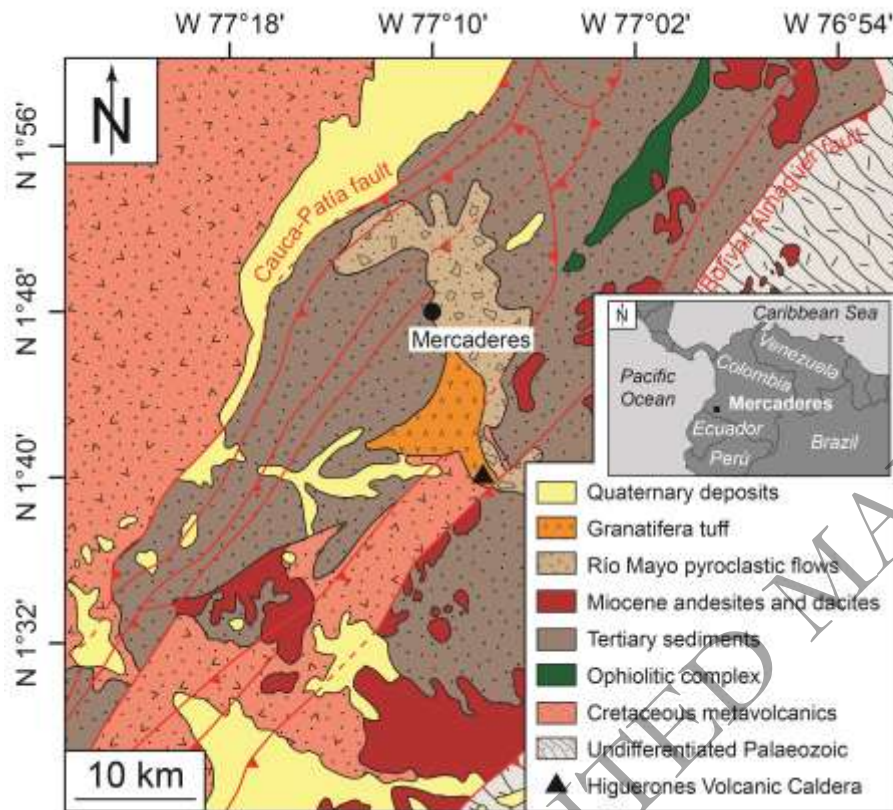
1474

1475

1476

1477

1478

1479

1480

1481

1482

1483

1484

1485

1486

1487

1488

1489   **Fig. 2.**

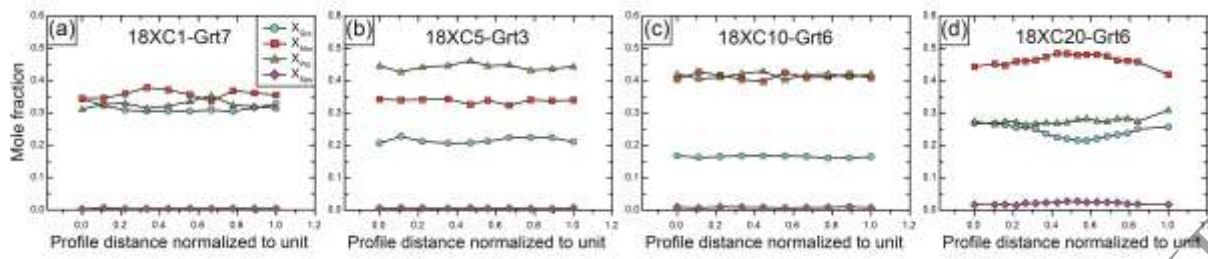1490

1491

1492

1493   **Fig. 3.**
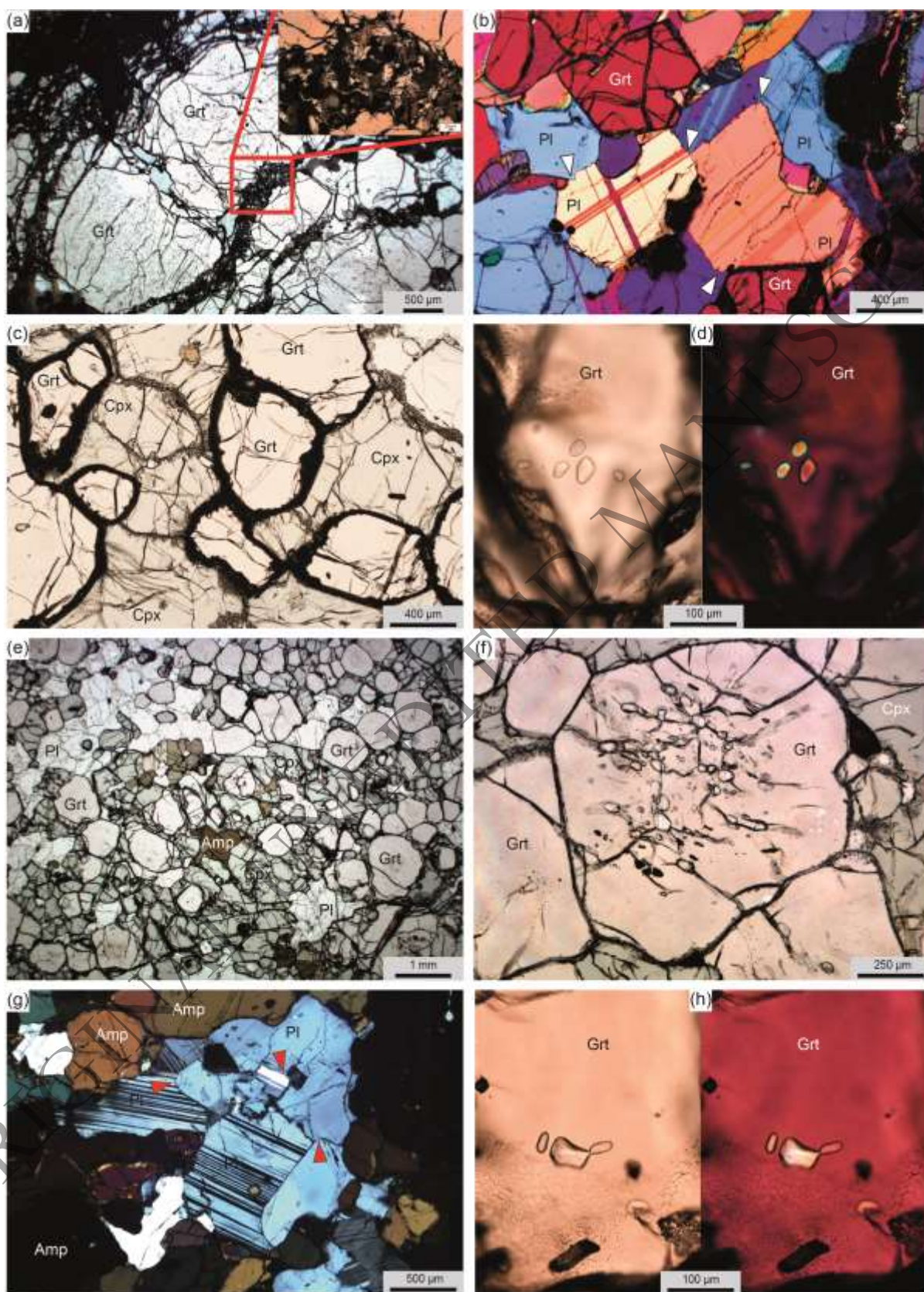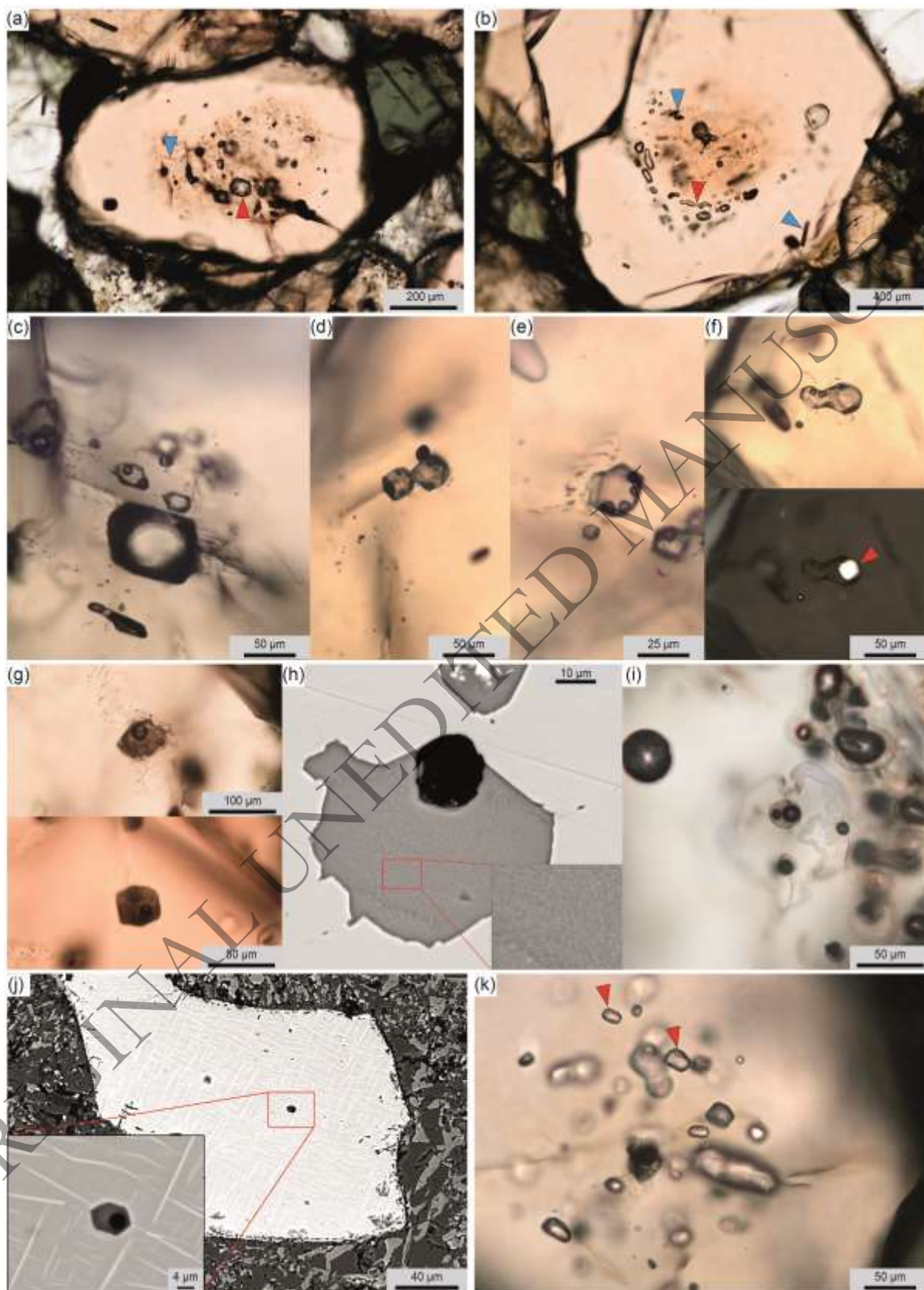
1494

1495
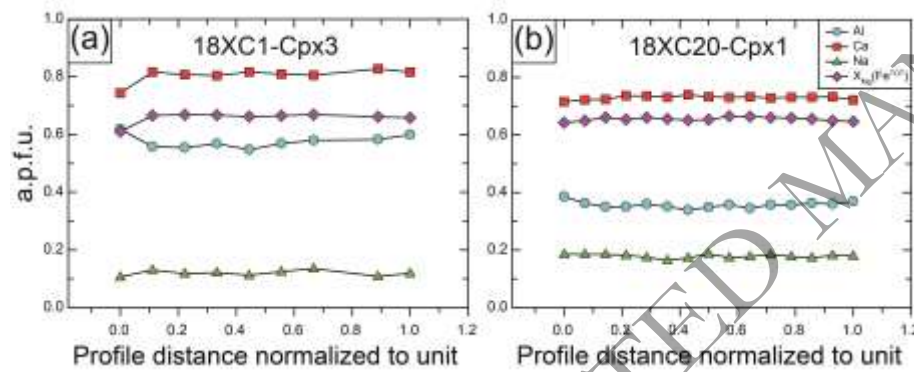
1496

1497   **Fig. 4.**
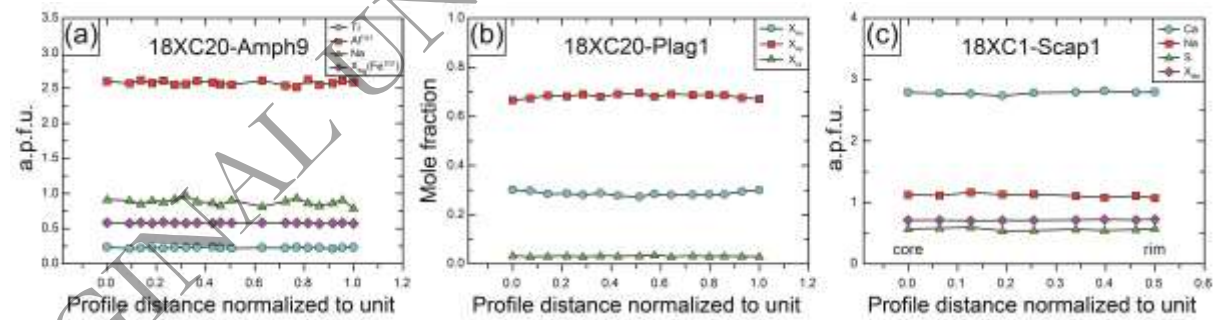

1498

1499

1500

1501   **Fig. 5.**

1502
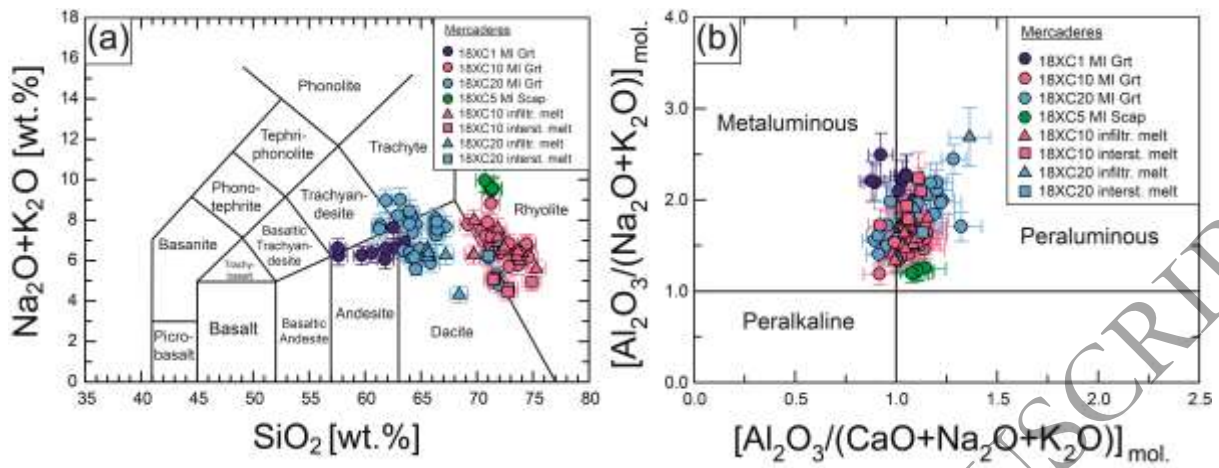
1503

1504

1505   **Fig. 6.**
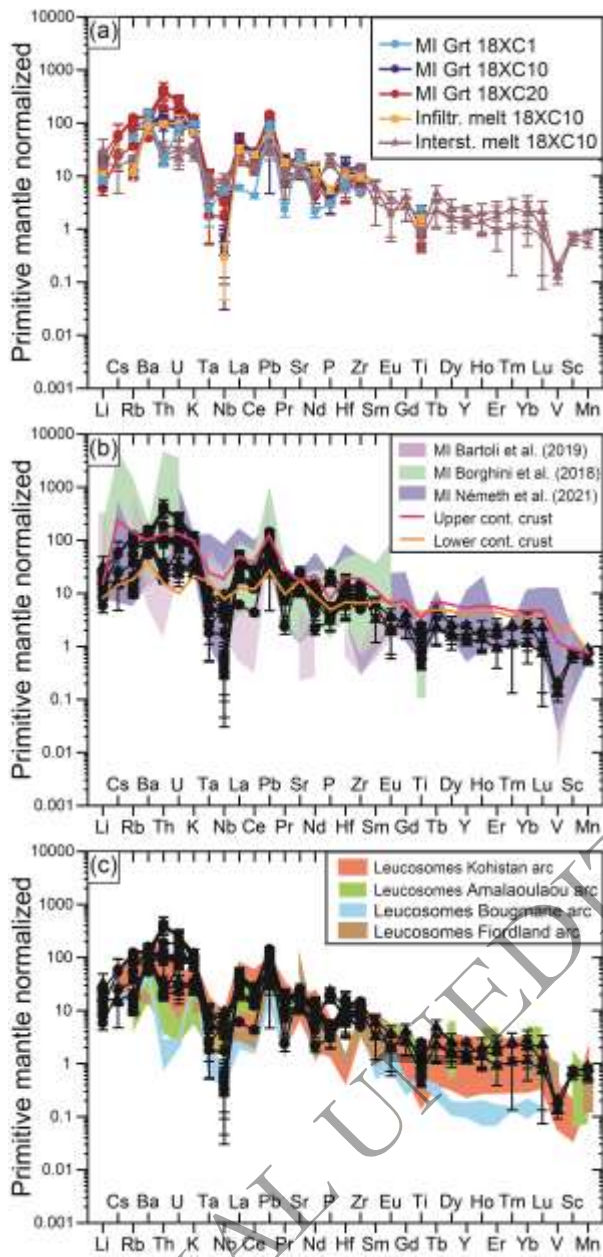

1506

1507

1508

1509

1510

1511

1512

1513

ORIGINAL UNEDITED MANUSCRIPT

1514 **Fig. 7.**

1515

1516

1517

1518

1519

1520

1521

1522

1523

1524

1525

1526

1527

1528

1529

1530

1531

1532

1533

1534

1535

1536

1537   **Fig. 8.**
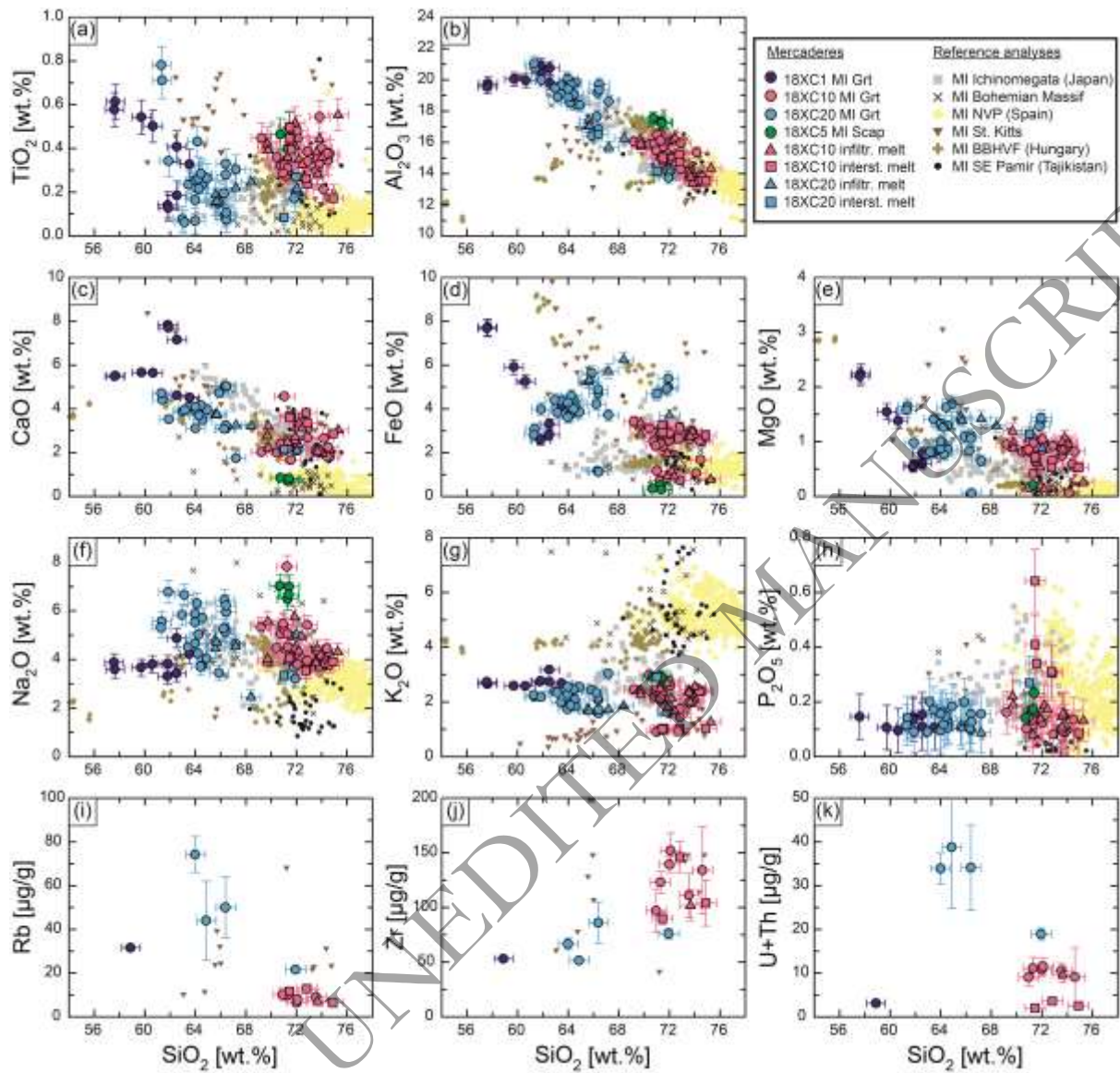
1538

1539

1540

1541

1542

1543

1544

1545

1546

1547

1548

1549   **Fig. 9.**

1550

1551

1552

1553

1554

1555

1556

1557

1558

1559
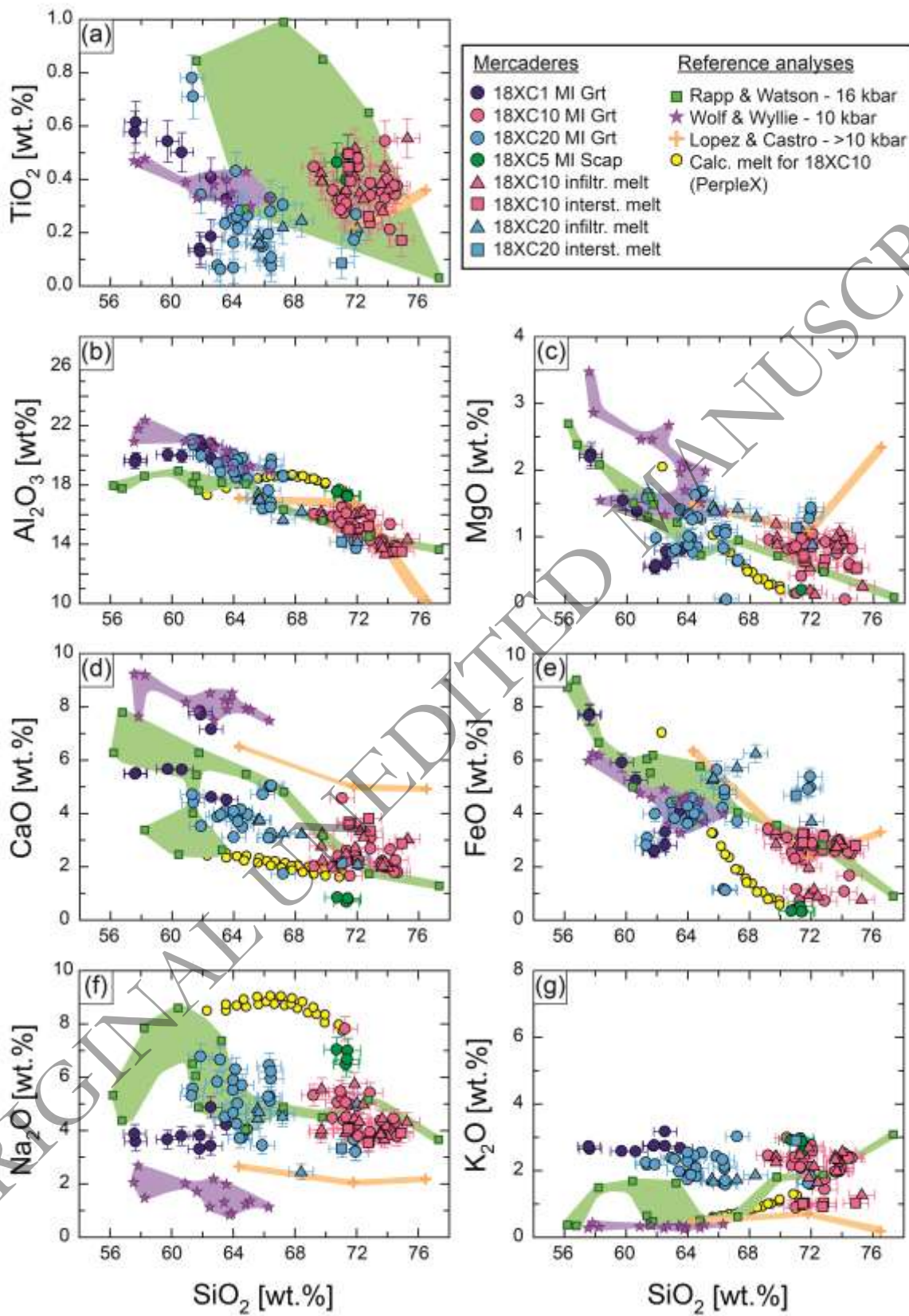
1560   **Fig. 10.**
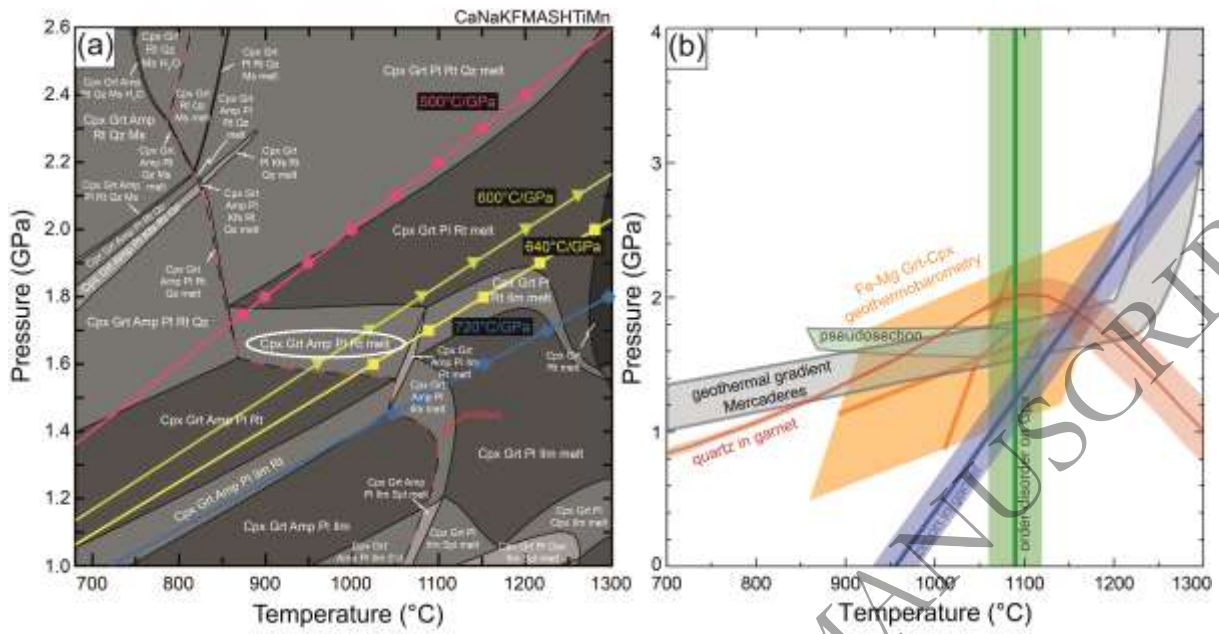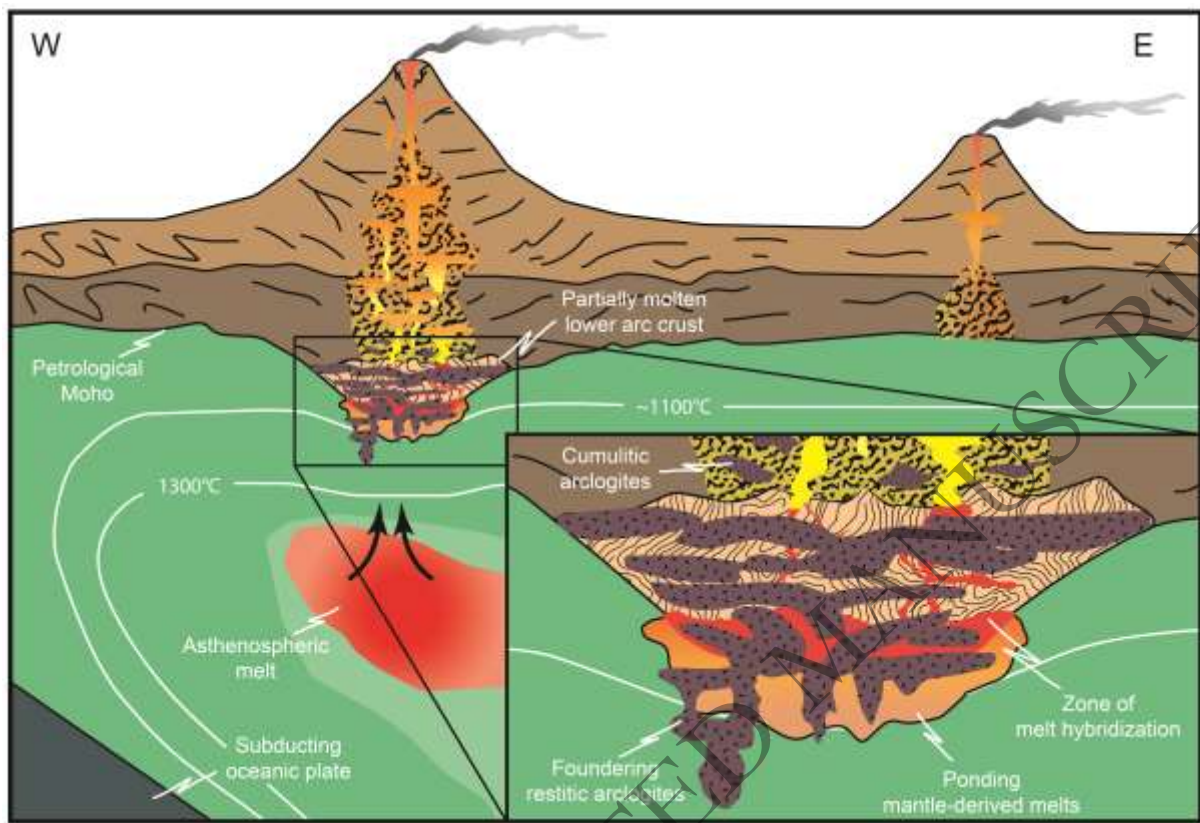

1561

1562

1563

1564   **Fig. 11.**

1565

1566

1567

1568   **Fig. 12.**

1569

1570

1571

1572 **Fig. 13.**

1573